INTERNATIONAL JOURNAL FOR NUMERICAL METHODS IN ENGINEERING
Int. J. Numer. Meth. Engng (2017)
Published online in Wiley Online Library (wileyonlinelibrary.com). DOI: 10.1002/nme.5476

Mixed Arlequin method for multiscale poromechanics problems

WaiChing Sun*,†, Zhijun Cai and Jinhyun Choo

Department of Civil Engineering and Engineering Mechanics, Columbia University in the City of New York, 614 SW Mudd, Mail Code: 4709 New York, NY, 10027, USA

SUMMARY

An Arlequin poromechanics model is introduced to simulate the hydro-mechanical coupling effects of fluid-infiltrated porous media across different spatial scales within a concurrent computational framework. A two-field poromechanics problem is first recast as the twofold saddle point of an incremental energy functional. We then introduce Lagrange multipliers and compatibility energy functionals to enforce the weak compatibility of hydro-mechanical responses in the overlapped domain. To examine the numerical stability of this hydro-mechanical Arlequin model, we derive a necessary condition for stability, the twofold inf–sup condition for multi-field problems, and establish a modified inf–sup test formulated in the product space of the solution field. We verify the implementation of the Arlequin poromechanics model through benchmark problems covering the entire range of drainage conditions. Through these numerical examples, we demonstrate the performance, robustness, and numerical stability of the Arlequin poromechanics model. Copyright © 2016 John Wiley & Sons, Ltd.

Received 1 November 2015; Revised 9 November 2016; Accepted 10 November 2016

KEY WORDS: poromechanics; multiscale simulations; domain coupling; Arlequin method; inf–sup tests

1. INTRODUCTION

The mechanical behavior of a fluid-infiltrated porous solid is significantly influenced by the presence and flow of fluid in the pores. While the flow of the pore fluid may introduce rate dependence to the mechanical responses of a porous medium, the deformation of solid skeleton may also displace pore fluid and lead to build up of excess pore pressure. This hydro-mechanical coupling appears in a variety of natural and engineered materials, ranging from rocks, soils, and concretes to bones and soft tissues. Reliable and efficient modeling of coupled hydro-mechanical processes in porous materials is thus crucial to address many engineering problems, such as unconventional energy recovery, hazards mitigation, and biomedical treatment [1–3]. Oftentimes, a major challenge in modeling these coupled hydro-mechanical processes is the demand to capture physical phenomena occurring at multiple length scales that span several orders of magnitude. As an example, let us consider hydraulic fractures in shale reservoirs. While these fractures are driven by fluid infiltration in nanometer-scale pores, the information crucial for engineering application is the impact of these fractures on the behavior and performance of kilometer-scale reservoirs. Nevertheless, due to its enormous computational costs, an explicit simulation of every grain-scale solid–fluid interaction in such a large-scale problem is impractical.

One feasible approach to incorporate small-scale dynamics into large-scale modeling is to make use of multiscale coupling techniques [4–6]. A variety of multiscale modeling methods have been developed and advanced over the past few decades in order to address interactions between microscopic and macroscopic responses. According to Aubertin et al. [7], these multiscale methods can be

*Correspondence to: WaiChing Sun, Assistant Professor, Department of Civil Engineering and Engineering Mechanics, Columbia University , 614 SW Mudd, Mail Code: 4709, New York, NY 10027.
†E-mail: wsun@columbia.edu

classified into three categories. The first category pertains to methods that model inherent multiscale characteristics by introducing a length scale through phenomenological laws. For instance, Fleck and Hutchinson [8] incorporate a strain gradient term into constitutive models such that multiple material length parameters can be defined for the field equations corresponding to different dominant mechanisms. Also, for capturing deformation bands much thinner than feasible mesh sizes, one can insert enhanced basis functions or localization elements to embed strong or weak discontinuous displacement fields [9–12].

The second category of multiscale methods is a class of hierarchical methods that incorporate micro-structural information from unit cells to compute effective (homogenized) properties of coarse (macroscopic) domains [13–18]. Kouznetsova et al. [19] present a gradient-enhanced homogenization scheme which obtains macroscopic stress, strain measure, and their gradients from solutions of boundary-value problems applied on representative volume elements. Ehlers et al. [20] describe a homogenization procedure that upscales higher-order kinematics of particle ensembles to both convectional stress measures and higher-order couple stresses. Liu et al. [15] apply a staggered nonlocal scheme to introduce a physical length scale for hierarchically coupled discrete elements–finite elements modeling of granular materials in a corotational framework. Another related application of homogenization-based multiscale methods has also been developed by several studies [4,5,21–23] to conduct large-scale flow simulations using tomographic images. The performance of these hierarchical multiscale methods relies on the existence of a representative elementary volume and the design of sequential coupling schemes to establish an exchange of information across scales.

Multiscale methods in the third category are concurrent methods that apply fine-scale, computationally demanding models to local region(s) of high interest (e.g., crack tip), while use coarse-scale, cost-efficient models elsewhere. Then, these methods extract high-resolution information in critical region(s) performing concurrent simulations of physical processes across length scales. In these concurrent simulations, the fine, critical domain is connected to the coarse, non-critical domain either via non-overlapped mortar interfaces (e.g., [24,25]) or overlapped handshaking domains (e.g., [26–30]). Previous work has successfully developed concurrent methods for coupling discrete and continuum models (e.g., [7,28,31]), classical local and non-local elastic continua (e.g., [32,33]), and structural elements with various mesh refinements (e.g., [27]).

The major upshot of concurrent multiscale approach is that it enables computational resources to be concentrated on region(s) of interest where important and complicated processes take place, without neglecting the far-field influence. Such efficient allocation of computational resources can significantly improve our modeling capabilities for a wide spectrum of problems whereby coupled hydro-mechanical processes occur across multiple spatial scales. Examples of these problems range from needle insertion into biological tissues [34], bone fractures [2], to hydraulic fracturing in unconventional reservoirs [35], and injection-induced seismic events [36]. Engineering designs and predictions for those applications can be substantially improved if numerical models can efficiently allocate computational resources to resolve the fine-scale information in the localized region of interest without neglecting the far-field influences.

In this work, we extend a concurrent multiscale method to simulate the coupled hydro-mechanical processes in fluid-infiltrated porous media across spatial scales. The proposed numerical model is based on the Arlequin framework, which was first proposed by Ben Dhia [26] as a general framework for coupling different domains and models. The Arlequin framework has been successfully applied to multiscale, multimodel simulations of a wide spectrum of multiscale solid mechanics problems (e.g., [27,29,33,37,38]). The theoretical basis and numerical tools to predict the spatial stability have been proposed in a few studies [28,33,38]. Each of these studies has proposed inf–sup tests for the corresponding boundary value problems. However, to the best of our knowledge, there is not yet any contribution dedicated to the extension of the Arlequin method to coupled hydro-mechanical problems. The new contributions of this work include a compatibility energy functional for spatial coupling of multiphase porous materials, a stability condition in the presence of both pore pressure and domain coupling constraints, a combined inf–sup test derived to examine the spatial stability using the product spaces of the displacement and pore pressure field, and numerical experiments that verify and demonstrate the robustness and accuracy of the Arlequin poromechanics model.

DOI: 10.1002/nme

The rest of this paper is organized as follows. In Section 2, we formulate the Arlequin poromechanics model, introducing a time-discrete variational statement and Lagrange multipliers for domain coupling. Subsequently, in Section 3, we derive a necessary condition for spatial stability of the developed method as a twofold inf–sup condition, and propose a new type of inf–sup test to evaluate the stability. In Section 4, we verify the developed Arlequin method in the entire range of drainage condition through two numerical examples. Then, we present a more complex example that showcases the performance of the method for coupling different models—particularly an isogeometric extended finite element model and a standard finite element model.

As for notations and symbols, bold-faced letters denote tensors; the symbol '$\cdot$' denotes a single contraction of adjacent indices of two tensors (e.g., $\boldsymbol{a}\cdot\boldsymbol{b}=a_ib_i$ or $\boldsymbol{c}\cdot\boldsymbol{d}=c_{ij}d_{jk}$); the symbol ':' denotes a double contraction of adjacent indices of tensor of rank two or higher (e.g., $\mathbb{C}:\boldsymbol{\epsilon}^{\boldsymbol{e}}=\mathbb{C}_{ijkl}\epsilon^{e}_{kl}$); the symbol '$\otimes$' denotes a juxtaposition of two vectors (e.g., $\boldsymbol{a}\otimes\boldsymbol{b}=a_ib_j$) or two symmetric second order tensors (e.g., $(\boldsymbol{\alpha}\otimes\boldsymbol{\beta})=\alpha_{ij}\beta_{kl}$). Following the standard sign convention in mechanics, stress is positive in tension.

2. MIXED ARLEQUIN FORMULATION FOR POROMECHANICS

This section presents a mixed Arlequin formulation for poromechanics problems. We begin by introducing the notion of domain partitioning that allows for the use of the Arlequin method. Governing equations of a coupled poromechanics problem are then reviewed briefly. To enforce the compatibility of solid and fluid motions between the sub-domains, we recast the coupled poromechanics problem as a saddle point problem of an incremental energy functional, and then apply partition of unity to the incremental energy density functional. Lastly, we derive the weak form and the matrix form of the Arlequin formulation.

2.1. Domain partitioning

Consider a two-phase porous medium that occupies a domain $\mathcal{B}\in\mathbb{R}^3$. To model critical and non-critical regions differently, we partition the domain $\mathcal{B}$ into a *coarse* sub-domain $\overline{\mathcal{B}}$ and a sub-domain $\tilde{\mathcal{B}}$ such that $\mathcal{B}=\overline{\mathcal{B}}\cup\tilde{\mathcal{B}}$, see Figure 1. Note that the two domains are overlapped in $\mathcal{B}^c=\overline{\mathcal{B}}\cap\tilde{\mathcal{B}}$. The coarse domain $\overline{\mathcal{B}}$ involves non-critical processes that can be well simulated by relatively simple models. Conversely, the fine domain $\tilde{\mathcal{B}}$ contains critical regions and it is usually (much) smaller than the coarse domain $\overline{\mathcal{B}}$. Therefore, we will concentrate more expensive, but more accurate models (e.g., a more advanced constitutive model, finer/higher-order discretization) on the fine domain. It is noted that even though the two models in the coarse and fine domains simulate the same physical processes in the overlapped domain, they do not need to be identical. For notational consistency, we shall denote quantities pertaining to $\overline{\mathcal{B}}$ and $\tilde{\mathcal{B}}$ by $\overline{(\cdot)}$ and $\tilde{(\cdot)}$, respectively (see Sun and Mota [33] for the same notation).

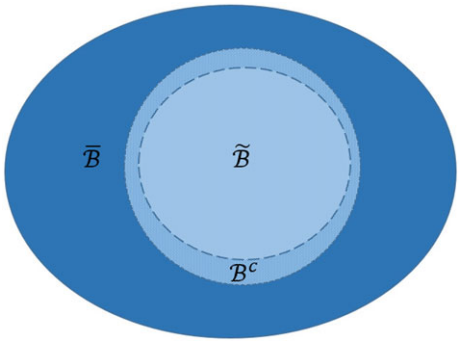

Figure 1. Partitioning of the domain $\mathcal{B}$ into a coarse domain $\overline{\mathcal{B}}$ and a fine domain $\tilde{\mathcal{B}}$. The coarse and fine domains are overlapped in $\mathcal{B}^c$.

DOI: 10.1002/nme

The boundary of the entire porous medium $\partial\mathcal{B}$ is also partitioned as

$$\partial\mathcal{B} = \partial\overline{\mathcal{B}} \cup \partial\tilde{\mathcal{B}}, \tag{2.1}$$

where $\partial\overline{\mathcal{B}}$ denotes the boundary of the coarse domain with the unit normal vector $\overline{\boldsymbol{n}}$, and $\partial\tilde{\mathcal{B}}$ the boundary of fine domain with the unit normal vector $\tilde{\boldsymbol{n}}$. Depending on the type of boundary conditions, the coarse domain boundary $\partial\overline{\mathcal{B}}$ is further decomposed as:

- $\partial_{\overline{\boldsymbol{u}}}\overline{\mathcal{B}}$: solid displacement boundary (Dirichlet).
- $\partial_{\overline{\boldsymbol{t}}}\overline{\mathcal{B}}$: solid traction boundary (Neumann).
- $\partial_{\overline{p}}\overline{\mathcal{B}}$: fluid pressure boundary (Dirichlet).
- $\partial_{\overline{\boldsymbol{q}}}\overline{\mathcal{B}}$: fluid flux boundary (Neumann).

Similarly, the fine domain boundary $\partial\tilde{\mathcal{B}}$ is also decomposed as

- $\partial_{\tilde{\boldsymbol{u}}}\tilde{\mathcal{B}}$: solid displacement boundary (Dirichlet).
- $\partial_{\tilde{\boldsymbol{t}}}\tilde{\mathcal{B}}$: solid traction boundary (Neumann).
- $\partial_{\tilde{p}}\tilde{\mathcal{B}}$: fluid pressure boundary (Dirichlet).
- $\partial_{\tilde{\boldsymbol{q}}}\tilde{\mathcal{B}}$: fluid flux boundary (Neumann).

The decompositions of $\partial\overline{\mathcal{B}}$ and $\partial\tilde{\mathcal{B}}$ are subjected to the following restrictions

$$\partial\overline{\mathcal{B}} = \partial_{\overline{\boldsymbol{u}}}\overline{\mathcal{B}} \cup \partial_{\overline{\boldsymbol{t}}}\overline{\mathcal{B}} = \partial_{\overline{p}}\overline{\mathcal{B}} \cup \partial_{\overline{\boldsymbol{q}}}\overline{\mathcal{B}}, \tag{2.2}$$

$$\partial\tilde{\mathcal{B}} = \partial_{\tilde{\boldsymbol{u}}}\tilde{\mathcal{B}} \cup \partial_{\tilde{\boldsymbol{t}}}\tilde{\mathcal{B}} = \partial_{\tilde{p}}\tilde{\mathcal{B}} \cup \partial_{\tilde{\boldsymbol{q}}}\tilde{\mathcal{B}}, \tag{2.3}$$

$$\emptyset = \partial_{\overline{\boldsymbol{u}}}\overline{\mathcal{B}} \cap \partial_{\overline{\boldsymbol{t}}}\overline{\mathcal{B}} = \partial_{\overline{p}}\overline{\mathcal{B}} \cap \partial_{\overline{\boldsymbol{q}}}\overline{\mathcal{B}}, \tag{2.4}$$

$$\emptyset = \partial_{\tilde{\boldsymbol{u}}}\tilde{\mathcal{B}} \cap \partial_{\tilde{\boldsymbol{t}}}\tilde{\mathcal{B}} = \partial_{\tilde{p}}\tilde{\mathcal{B}} \cap \partial_{\tilde{\boldsymbol{q}}}\tilde{\mathcal{B}}. \tag{2.5}$$

The solid displacement boundary of the entire domain is the union of the solid displacement boundaries of the coarse and fine domains, that is, $\partial_{\boldsymbol{u}}\mathcal{B} = \partial_{\overline{\boldsymbol{u}}}\overline{\mathcal{B}} \cup \partial_{\tilde{\boldsymbol{u}}}\tilde{\mathcal{B}}$. Similarly, the union of the fluid pressure boundaries of the coarse and fine domains forms the entire fluid pressure boundary, that is, $\partial_p\mathcal{B} = \partial_{\overline{p}}\overline{\mathcal{B}} \cup \partial_{\tilde{p}}\tilde{\mathcal{B}}$. Note that in both cases, the coarse and fine domains can have overlapped Dirichlet boundaries, that is, $\partial_{\boldsymbol{u}}\mathcal{B}^c = \partial_{\overline{\boldsymbol{u}}}\overline{\mathcal{B}} \cap \partial_{\tilde{\boldsymbol{u}}}\tilde{\mathcal{B}} \neq \emptyset$ and $\partial_p\mathcal{B}^c = \partial_{\overline{p}}\overline{\mathcal{B}} \cap \partial_{\tilde{p}}\tilde{\mathcal{B}} \neq \emptyset$. Similarly, the solid traction boundary of the entire domain is partitioned as $\partial_{\boldsymbol{t}}\mathcal{B} = \partial_{\overline{\boldsymbol{t}}}\overline{\mathcal{B}} \cup \partial_{\tilde{\boldsymbol{t}}}\tilde{\mathcal{B}}$ with an overlapped boundary $\partial_{\boldsymbol{t}}\mathcal{B}^c = \partial_{\overline{\boldsymbol{t}}}\overline{\mathcal{B}} \cap \partial_{\tilde{\boldsymbol{t}}}\tilde{\mathcal{B}}$, and the fluid flux boundary as $\partial_{\boldsymbol{q}}\mathcal{B} = \partial_{\overline{\boldsymbol{q}}}\overline{\mathcal{B}} \cup \partial_{\tilde{\boldsymbol{q}}}\tilde{\mathcal{B}}$ with an overlapped boundary $\partial_{\boldsymbol{q}}\mathcal{B}^c = \partial_{\overline{\boldsymbol{q}}}\overline{\mathcal{B}} \cap \partial_{\tilde{\boldsymbol{q}}}\tilde{\mathcal{B}}$. To enforce the compatibility between the fluid and solid motions of the coarse and fine domains, we will introduce Lagrange multipliers to the sub-domains $\mathcal{B} \setminus \partial_{\boldsymbol{u}}\mathcal{B}$ (for the solid displacement) and $\mathcal{B} \setminus \partial_p\mathcal{B}$ (for the fluid pressure).

Finally, the initial conditions at $t = 0$ are given by $\{\overline{\boldsymbol{u}}_o, \overline{p}_o\}$ for the coarse domain and $\{\tilde{\boldsymbol{u}}_o, \tilde{p}_o\}$ for the fine domain.

2.2. *Field equations for poromechanics problems*

In this work, our goal is to model *coupled fluid-diffusion–solid-deformation processes* in fluid-saturated porous media. The formulation of the poromechanics model for fluid-saturated porous media has been well established in the literature. Readers interested in the details of the poromechanics theory are referred to standard texts such as [1,3,39]. Here, we provide a brief overview of the subject for completeness.

In a nutshell, the continuum poromechanics model conceptualizes the fluid-infiltrated porous media as a continuum mixture of the solid and fluid constituents, each occupies a fraction of volume in the macroscopic body. Provided that a representative elementary volume exists, the behavior of porous media can be predicted by introducing proper constitutive laws for the solid skeleton and pore fluid flow as well as imposing conservation laws for linear momentum and mass as field equations. For simplicity, here we consider the case in which the pore space is filled up with a single-phase fluid (e.g., water). Therefore, in what follows, we consider a two-phase continuum composed of one

DOI: 10.1002/nme

solid and one fluid constituents. In addition, the following assumptions are made to further simplify the problem:

1. The isothermal condition holds.
2. The inertial effect is negligible.
3. There is no mass exchange between the solid and fluid constituents.
4. Reynold's number of the flow in the pore space is sufficiently low such that convection is negligible.
5. Darcy's law is valid.
6. The deformation of the solid skeleton is elastic, isotropic, and infinitesimal.
7. The effective stress principle is valid.
8. The pore space is fully saturated by a single type of fluid.

The balance of linear momentum of the two-phase porous media then reads

$$\nabla \cdot \ (\boldsymbol{\sigma}' - \boldsymbol{B}p) + \boldsymbol{\gamma} = \boldsymbol{0}, \tag{2.6}$$

where $\boldsymbol{\sigma}'$ is the effective stress, p is the pore pressure, and $\boldsymbol{\gamma}$ is the body force vector. The second-order tensor $\boldsymbol{B}$ is a generalization of Biot's coefficient in the isotropic elasticity case. For the linear elasticity case, $\boldsymbol{B}$ may read (cf. [40]),

$$\boldsymbol{B} = \boldsymbol{I} - \frac{1}{3K_s}\mathbb{C}_{\text{sk}} : \boldsymbol{I}, \tag{2.7}$$

where K_s is the intrinsic bulk modulus of the solid constituent, $\mathbb{C}_{\text{sk}}$ is the fourth-order elasticity tensor, and $\boldsymbol{I}$ is the second-order identity tensor. Note that in the isotropic case, this expression simplifies to the classical expression of Biots coefficient $\boldsymbol{B} = B\boldsymbol{I} = (1 - K/K_s)\boldsymbol{I}$ where K is the bulk modulus of the solid matrix (cf. [3,41–43]). Thus, in this work, we consider the effective stress of the form

$$\boldsymbol{\sigma}' = \boldsymbol{\sigma} + Bp\boldsymbol{I}, \tag{2.8}$$

where $\boldsymbol{\sigma}$ is the total stress in the porous medium. When the solid deformation is infinitesimal and hyperelastic, constitutive law for the solid skeleton can be expressed as

$$\boldsymbol{\sigma}' = \frac{\partial W(\boldsymbol{\epsilon})}{\partial \boldsymbol{\epsilon}}, \tag{2.9}$$

where $W(\boldsymbol{\epsilon})$ is the stored energy function of the solid skeleton. The infinitesimal strain tensor of the solid skeleton $\boldsymbol{\epsilon}$ reads,

$$\boldsymbol{\epsilon} = \nabla^{\text{sym}}\boldsymbol{u} = \frac{1}{2}(\nabla \boldsymbol{u} + \nabla^{\text{T}}\boldsymbol{u}). \tag{2.10}$$

The corresponding incremental form of the solid constitutive relation in (2.9) is given by

$$\Delta\boldsymbol{\sigma}' = \mathbb{D} : \Delta\boldsymbol{\epsilon} \tag{2.11}$$

where $\mathbb{D}$ is a fourth-order tensor of tangent stiffness tensor. If the solid skeleton exhibits linear isotropic elastic behavior, then $\mathbb{D} = \mathbb{C}_{\text{sk}}$. For soils and soft rocks Biot's coefficient $B \approx 1$, whereas for hard rocks or biological materials B is usually less than one. Finally, the body force $\boldsymbol{\gamma}$ acting on the mixture of the solid matrix and the pore fluid is given by

$$\boldsymbol{\gamma} = \boldsymbol{\gamma}^s + \boldsymbol{\gamma}^f = (1 - \phi^f)\rho_s\boldsymbol{g} + \phi^f\rho_f\boldsymbol{g}, \tag{2.12}$$

where ϕ^f is the porosity (the volume fraction of the pore fluid), ρ_s and ρ_f are the intrinsic densities of the solid and fluid constituents, respectively, and $\boldsymbol{g}$ is the gravitational acceleration. The balance of mass with compressible fluid and solid constituents reads,

$$\frac{1}{M}\dot{p} + B\nabla \cdot \ \dot{\boldsymbol{u}} + \nabla \cdot \ \boldsymbol{q} = 0, \tag{2.13}$$

DOI: 10.1002/nme

where M is Biot's modulus and $\boldsymbol{q}$ is the seepage velocity. For fully saturated, isotropic porous materials, M may be related to the intrinsic bulk moduli and porosity as follows [40,42,43]:

$$M = \frac{K_s K_f}{K_f(B - \phi^f) + K_s \phi^f}. \tag{2.14}$$

If the flow in the pore space remains laminar and the fluid movement is dominated by viscous forces, then the seepage velocity and the gradient of the pore pressure can be related by Darcy's law,

$$\boldsymbol{q} = -\frac{1}{\mu}\boldsymbol{k} \cdot (\nabla p - \rho_f \boldsymbol{g}), \tag{2.15}$$

where $\boldsymbol{k}$ is the effective permeability and μ is the dynamic viscosity of the pore fluid. In this work, we shall assume isotropic permeability, that is, $\boldsymbol{k} = k\boldsymbol{I}$. Substituting this equation into (2.13) leads to

$$\frac{1}{M}\dot{p} + B\nabla \cdot \dot{\boldsymbol{u}} - \nabla \cdot \frac{1}{\mu}\boldsymbol{k}(\nabla p - \rho_f \boldsymbol{g}) = 0. \tag{2.16}$$

Observe that the two governing Eqs. (2.6) and (2.16) have two unknowns—the solid displacement $\boldsymbol{u}$ and the pore pressure p. For this reason, this formulation is often referred to as a $\boldsymbol{u}/p$ formulation (cf. [1,16,44,45]). Alternatively, it is also possible to formulate a poromechanics problem in terms of fluid mass flux vector and solid displacement unknowns (cf. [46,47]) or in terms of Darcy's velocity, solid displacement, and pore pressure (cf. [1,48,49]). The application of the Arlequin framework for the latter two formulations (i.e., $\boldsymbol{u}/\boldsymbol{v}$ and $\boldsymbol{u}/\boldsymbol{v}/p$) is not considered herein, and will be considered in future studies.

2.3. Variational statement for poromechanics

The goal of this section is to derive a time-discrete weak form of the poromechanics problem, which will then serve as the basis for the derivation of the Arlequin poromechanics model presented in Section 2.4. In previous works, such as [1,45,50–52], the finite element model for the poromechanics problem is often formulated via a weight-residual argument. An alternative approach has been explored by Biot [53] and Armero and Callari [10] who consider the porous medium an open system in which field equations can be recast as the Euler–Lagrange equation from a generalization of d'Alembert's principle. While both approaches may lead to the same set of field equations, here we adopt the latter approach in order to obtain an equivalent static problem between two incremental time steps before discretizing the spatial domain. An upshot of this approach is that it makes the solutions of the equivalent static problem corresponding to an incremental saddle point energy functional, hence allowing us to formulate the Arlequin poromechanics model via the energy blending approach. Nevertheless, it should be noted that the Arlequin formulation may also be introduced by using virtual work principle as the starting point, as performed in the pioneering work by Ben Dhia [26] which first introduced the Arlequin method. Our goal here is to derive a time-discrete energy functional of which the corresponding Euler–Lagrange equation is the time-discrete weak form of the field equation presented in (2.6) and (2.16). In Section 2.4, we will show that the Arlequin poromechanics problem can be formulated by applying partition of unity to the incremental energy functional and introducing an additional energy functional to impose compatibility constraints in the overlapped domain(s).

To derive a variational statement, we first introduce two spaces for the trial functions for the displacement and pore pressure fields, that is,

$$\boldsymbol{V}_{\boldsymbol{u}} = \{\boldsymbol{u} : \mathcal{B} \to \mathbb{R}^3 | \boldsymbol{u} \in [H^1(\mathcal{B})]^3, \boldsymbol{u}|_{\partial_{\boldsymbol{u}}\mathcal{B}} = \boldsymbol{u}_{\text{pred}}\}, \tag{2.17}$$

$$\boldsymbol{V}_p = \{p : \mathcal{B} \to \mathbb{R} | p \in [H^1(\mathcal{B})], p|_{\partial_p\mathcal{B}} = p_{\text{pred}}\}, \tag{2.18}$$

DOI: 10.1002/nme

where H^1 denotes the Sobolev space of degree one, $\boldsymbol{u}_{\text{pred}}$ and p_{pred} represent the prescribed boundary values of the solid displacement and pore pressure, respectively. Accordingly, we also define admissible variations of displacement $\delta\boldsymbol{u}$ and pore pressure δp as

$$\boldsymbol{V}_{\delta\boldsymbol{u}} = \{\delta\boldsymbol{u} : \mathcal{B} \to \mathbb{R}^3 | \delta\boldsymbol{u} \in [H^1(\mathcal{B})]^3, \delta\boldsymbol{u}|_{\partial_u\mathcal{B}} = \boldsymbol{0}\}, \tag{2.19}$$

$$\boldsymbol{V}_{\delta p} = \{\delta p : \mathcal{B} \to \mathbb{R} | \delta p \in [H^1(\mathcal{B})], \delta p|_{\partial_p\mathcal{B}} = 0\}. \tag{2.20}$$

To obtain an incremental energy functional of the poromechanics problem, we adopt an approach used in other variational frameworks [54–57] that performs temporal discretization first and then spatial discretization. In fact, this discretization sequence is the opposite to the typical sequence in poromechanics formulations (e.g., [16,50,58–60]) whereby the spatial domain is discretized first. Yet, this typical sequence does not allow us to derive an incremental energy functional necessary for the Arlequin formulation. Therefore, we first discretize the time domain as $[0, T] = \cup_{n=0}^{N}[t_n, t_{n+1}] \in \mathbb{R}^+$. Then, our objective is the following: Given variables at the previous time step t_n, obtain an incremental update for the solid displacement and fluid pressure at time step t_{n+1}. Hereafter, we will use the backward Euler method and assume that Biot's coefficient B, Biot's modulus M, and the permeability $\boldsymbol{k}$ are constant.

We formulate a discrete Lagrangian such that the updated solid displacement and fluid pressure $(\boldsymbol{u}_{n+1}, p_{n+1})$ satisfying the time-discrete versions of (2.6) and (2.16) are the saddle point of the the discrete energy functional. The total (discrete) free energy functional of the solid matrix Π^s at time t_{n+1} is the total free energy of the porous media subtracted by the total free energy contributed by the pore fluid of the same control volume [61],

$$\mathit{\Pi}[\boldsymbol{u}_{n+1}, p_{n+1}]_{n+1} = \mathit{\Pi}^s[\boldsymbol{u}_{n+1}, p_{n+1}]_{n+1} - \mathit{\Pi}^f[\boldsymbol{u}_{n+1}, p_{n+1}]_{n+1} + \mathit{\Pi}^{\text{ext}}[\boldsymbol{u}_{n+1}, p_{n+1}]_{n+1}. \tag{2.21}$$

Under the quasi-static and isothermal conditions, the internal energy of the solid matrix at time $t = t_{n+1}$ is given by [62,63]

$$\mathit{\Pi}^s[\boldsymbol{u}_{n+1}, p_{n+1}]_{n+1} = \frac{1}{2}\int_{\mathcal{B}} (\boldsymbol{\sigma}'_{n+1}) : \nabla^{\text{sym}}\boldsymbol{u}_{n+1}\, dV, \tag{2.22}$$

where $\Delta t = t_{n+1} - t_n$ is the time increment. The energy contribution of the pore fluid at time $t = t_{n+1}$ is given by

$$\mathit{\Pi}^f[\boldsymbol{u}_{n+1}, p_{n+1}]_{n+1} = \mathit{\Pi}^f[\boldsymbol{u}_n, p_n]_n + \int_{\mathcal{B}} \frac{(p_{n+1} - p_n)^2}{2M} + Bp_{n+1}\boldsymbol{I} : (\nabla^{\text{sym}}\boldsymbol{u}_{n+1} - \nabla^{\text{sym}}\boldsymbol{u}_n)\, dV, \tag{2.23}$$

and the external work at $t = t_{n+1}$ is

$$\mathit{\Pi}^{\text{ext}}[\boldsymbol{u}_{n+1}, p_{n+1}]_{n+1} = -\int_{\partial_q\mathcal{B}} \hat{\boldsymbol{q}} \cdot \boldsymbol{n}\, \overline{p}_{n+1} d\mathit{\Gamma} - \int_{\partial_t\mathcal{B}} \hat{\boldsymbol{t}} \cdot \boldsymbol{u}_{n+1} d\mathit{\Gamma} - \int_{\mathcal{B}} \boldsymbol{\gamma} \cdot \boldsymbol{u}_{n+1}\, dV, \tag{2.24}$$

where $\hat{\boldsymbol{q}}$ and $\hat{\boldsymbol{t}}$ are the prescribed fluid flux and traction, respectively. The dissipation due to seepage of the pore fluid at time $t = t_{n+1}$ is approximated by the backward Euler method, that is,

$$\mathit{\Omega}[p_{n+1}]|_n^{n+1} \approx \int_{\mathcal{B}} \frac{\Delta t}{2\mu}(\nabla p_{n+1} - \rho_f \boldsymbol{g}) \cdot \boldsymbol{k} \cdot (\nabla p_{n+1} - \rho_f \boldsymbol{g})\, dV, \tag{2.25}$$

where the effective permeability tensor $\boldsymbol{k}$ is assumed to be symmetric and positive semi-definite. The discrete Lagrangian $H[\boldsymbol{u}_{n+1}, p_{n+1}]_{n+1}$ is therefore given by

$$H[\boldsymbol{u}_{n+1}, p_{n+1}]_{n+1} = \mathit{\Pi}[\boldsymbol{u}_{n+1}, p_{n+1}]_{n+1} - \mathit{\Pi}[\boldsymbol{u}_n, p_n]_n - \mathit{\Omega}[p_{n+1}]|_n^{n+1}. \tag{2.26}$$

DOI: 10.1002/nme

The first variation that corresponds to the saddle point of the incremental energy functional with respect to the incremental solution field $(\boldsymbol{u}_{n+1}, p_{n+1})$ reads,

$$D\,H[\delta\boldsymbol{u}]_{n+1} = \int_{\mathcal{B}} (\boldsymbol{\sigma}'_{n+1} : \nabla^{\mathrm{sym}}\delta\boldsymbol{u} - Bp_{n+1}\nabla\cdot\delta\boldsymbol{u} - \boldsymbol{\gamma}\delta\boldsymbol{u})\,dV - \int_{\partial_t\mathcal{B}} \hat{\boldsymbol{t}}\cdot\delta\boldsymbol{u}\,d\Gamma, \tag{2.27}$$

$$\begin{aligned} D\,H[\delta p]_{n+1} = &\int_{\mathcal{B}} \left(\frac{1}{M}(p_{n+1}-p_n)\delta p + B\nabla\cdot\,(\boldsymbol{u}_{n+1}-\boldsymbol{u}_n)\delta p - \Delta t\nabla\cdot\,\frac{1}{\mu}\boldsymbol{k}\cdot(\nabla p_{n+1}+\rho\boldsymbol{g})\delta p \right) dV \\ &- \int_{\partial_q\mathcal{B}} \hat{\boldsymbol{q}}\cdot\boldsymbol{n}\;\delta p\;d\Gamma = 0, \end{aligned} \tag{2.28}$$

where the operator $D(\cdot)$ denotes the Gateaux derivative, that is, $DH(\delta\boldsymbol{u}) = \frac{d}{d\eta}H(\boldsymbol{u}+\eta\delta\boldsymbol{u})|_{\eta=0}$. Note that the system of equations listed in (2.27)–(2.28) may also be obtained by the weight-residual method. In this case, the starting point is to use (2.6) and (2.16) as the strong form. Then, a weak form of the linear momentum and mass conservation equations can be obtained using a weight-residual argument and integration by parts with testing functions $(\boldsymbol{\delta u}, \delta p)$, followed by a discretization in the temporal domain typically performed by a one-step or linear multi-step method (cf. [64]). For brevity, this derivation is not repeated in this work. Interested readers may refer to [1,2,45,51,52,64,65] for details.

2.4. Variational statement for Arlequin poromechanics

We now enforce the compatibility of the mechanical and hydrological states in the overlapped domain. The Arlequin framework enforces the compatibility by suitably partitioning the energy of the overlapped domain into the associated sub-domains. Following this approach, here we formulate a variational statement for the Arlequin poromechanics. For simplicity, we restrict our focus on a sub-class of the Arlequin poromechanics problem where the overlapped domain consists of only two models, which are referred to as coarse and fine models. In this case, the Arlequin model for the poromechanics problem can be established by: (1) applying partition of unity to the coarse and fine incremental energy functionals, and (2) introducing constraints and Lagrange multipliers to enforce compatibility.

Recall the notation $\overline{(\cdot)}$ for the coarse domain and $\tilde{(\cdot)}$ for the fine domain. We define the trial spaces as

$$\boldsymbol{V}_{\overline{\boldsymbol{u}}} = \{\overline{\boldsymbol{u}} : \mathcal{B}\to\mathbb{R}^3 | \overline{\boldsymbol{u}} \in [H^1(\mathcal{B})]^3, \overline{\boldsymbol{u}}|_{\partial_{\overline{u}}\mathcal{B}} = \overline{\boldsymbol{u}}_{\mathrm{pred}}\} \tag{2.29}$$

$$\boldsymbol{V}_{\overline{p}} = \{\overline{p} : \mathcal{B}\to\mathbb{R} | \overline{p} \in [H^1(\mathcal{B})], \overline{p}|_{\partial_{\overline{p}}\mathcal{B}} = \overline{p}_{\mathrm{pred}}\} \tag{2.30}$$

$$\boldsymbol{V}_{\tilde{\boldsymbol{u}}} = \{\tilde{\boldsymbol{u}} : \mathcal{B}\to\mathbb{R}^3 | \tilde{\boldsymbol{u}} \in [H^1(\mathcal{B})]^3, \tilde{\boldsymbol{u}}|_{\partial_{\tilde{u}}\mathcal{B}} = \tilde{\boldsymbol{u}}_{\mathrm{pred}}\} \tag{2.31}$$

$$\boldsymbol{V}_{\tilde{p}} = \{\tilde{p} : \mathcal{B}\to\mathbb{R} | \tilde{p} \in [H^1(\mathcal{B})], \tilde{p}|_{\partial_{\tilde{p}}\mathcal{B}} = \tilde{p}_{\mathrm{pred}}\}. \tag{2.32}$$

The admissible variations of displacement and pore pressure for the coarse and fine domains are defined as

$$\boldsymbol{V}_{\delta\overline{\boldsymbol{u}}} = \{\delta\overline{\boldsymbol{u}} : \mathcal{B}\to\mathbb{R}^3 | \delta\overline{\boldsymbol{u}} \in [H^1(\mathcal{B})]^3, \delta\overline{\boldsymbol{u}}|_{\partial_{\overline{u}}\mathcal{B}} = \boldsymbol{0}\} \tag{2.33}$$

$$\boldsymbol{V}_{\delta\overline{p}} = \{\delta\overline{p} : \mathcal{B}\to\mathbb{R} | \delta\overline{p} \in [H^1(\mathcal{B})], \delta\overline{p}|_{\partial_{\overline{p}}\mathcal{B}} = 0\} \tag{2.34}$$

$$\boldsymbol{V}_{\delta\tilde{\boldsymbol{u}}} = \{\delta\tilde{\boldsymbol{u}} : \mathcal{B}\to\mathbb{R}^3 | \delta\tilde{\boldsymbol{u}} \in [H^1(\mathcal{B})]^3, \delta\tilde{\boldsymbol{u}}|_{\partial_{\tilde{u}}\mathcal{B}} = \boldsymbol{0}\} \tag{2.35}$$

$$\boldsymbol{V}_{\delta\tilde{p}} = \{\delta\tilde{p} : \mathcal{B}\to\mathbb{R} | \delta\tilde{p} \in [H^1(\mathcal{B})], \delta\tilde{p}|_{\partial_{\tilde{p}}\mathcal{B}} = 0\}. \tag{2.36}$$

DOI: 10.1002/nme

In the Arlequin framework, multiple models are used to simulate the same physical processes in the overlapped domain. Accordingly, the energy of the system in the overlapped domain is partitioned into the sub-domains by a weighting function $\chi : \mathcal{B} \to [0, 1]$. This weighting function can be chosen as discontinuous, piece-wise constant or polynomials of various orders of completeness in space, provided that partition of unity is satisfied [27,33]. For instance, in a one-dimensional problem, if $\mathcal{B}^c = [a, b] \in \mathcal{B}$ and $\mathcal{B} \setminus \mathcal{B}^c = [0, a[\in \mathcal{B}$, then the weighting function χ can be defined as:

$$\chi(\mathbf{x}) = \begin{cases} 0 \ , & \text{for } \mathbf{x} \in \overline{\mathcal{B}} \setminus \mathcal{B}^c \ , \\ \frac{x}{b-a} - \frac{a}{b-a} \ , & \text{for } \mathbf{x} \in \mathcal{B}^c \ , \\ 1 \ , & \text{for } \mathbf{x} \in \tilde{\mathcal{B}} \setminus \mathcal{B}^c \ . \end{cases} \tag{2.37}$$

For notational brevity, we define $\boldsymbol{\varphi}_u = \{\overline{\boldsymbol{u}}, \tilde{\boldsymbol{u}}\}$ and $\boldsymbol{\varphi}_p = \{\overline{p}, \tilde{p}\}$. Then, the total free energy and viscous dissipation are the linear combination of the coarse and fine energy functionals that are partitioned via the weighting function χ, that is,

$$\Pi^s_{Ar}[\boldsymbol{\varphi}_{u,n+1}, \boldsymbol{\varphi}_{p,n+1}]_{n+1} = (1-\chi)\overline{\Pi}^s[\overline{\boldsymbol{u}}_{n+1}, \overline{p}_{n+1}]_{n+1} + \chi\tilde{\Pi}^s[\tilde{\boldsymbol{u}}_{n+1}, \tilde{p}_{n+1}]_{n+1}, \tag{2.38}$$

$$\Pi^f_{Ar}[\boldsymbol{\varphi}_{u,n+1}, \boldsymbol{\varphi}_{p,n+1}]_{n+1} = (1-\chi)\overline{\Pi}^f[\overline{\boldsymbol{u}}_{n+1}, \overline{p}_{n+1}]_{n+1} + \chi\tilde{\Pi}^f[\tilde{\boldsymbol{u}}_{n+1}, \tilde{p}_{n+1}]_{n+1}, \tag{2.39}$$

$$\Pi^{\text{ext}}_{Ar}[\boldsymbol{\varphi}_{u,n+1}, \boldsymbol{\varphi}_{p,n+1}]_{n+1} = (1-\chi)\overline{\Pi}^{\text{ext}}[\overline{\boldsymbol{u}}_{n+1}, \overline{p}_{n+1}]_{n+1} + \chi\tilde{\Pi}^{\text{ext}}[\tilde{\boldsymbol{u}}_{n+1}, \tilde{p}_{n+1}]_{n+1}, \tag{2.40}$$

$$\Omega[p_{n+1}]|_{n+1} = (1-\chi)\overline{D}[\overline{p}_{n+1}]|_{n+1} + (\chi)\tilde{D}[\tilde{p}_{n+1}]|_{n+1}. \tag{2.41}$$

Note that in previous work such as [27,66], the weighting functions of the external work and the internal work are not necessarily identical. Nevertheless, we choose to use the same weighting function χ to simplify the formulation. Therefore, we can write the expression for the total energy of the porous medium in the context of the Arlequin framework as

$$\begin{aligned} \Pi_{Ar}[\boldsymbol{\varphi}_{u,n+1}, \boldsymbol{\varphi}_{p,n+1}]_{n+1} &= \Pi^s_{Ar} - \Pi^f_{Ar} + \Pi^{\text{ext}}_{Ar} \\ &= \chi\overline{\Pi}_{Ar}[\overline{\boldsymbol{u}}_{n+1}, \overline{p}_{n+1}]_{n+1} + (1-\chi)\tilde{\Pi}_{Ar}[\tilde{\boldsymbol{u}}_{n+1}, \tilde{p}_{n+1}]_{n+1}. \end{aligned} \tag{2.42}$$

To enforce the compatibility between the coarse and fine solutions in the overlapped domain, the Arlequin incremental energy functionals must be augmented by constraints that minimize the discrepancies of the coarse and fine solutions. The pioneering work by Ben Dhia [67] and follow-up analyses such as [28,33,66] have analyzed various ways to enforce the compatibility for displacement-based finite element models. These studies have commonly found that a constraint that minimizes the displacement discrepancy measured by the H^1 norm seems to yield the most stable and accurate formulation. In this work, we extend this H^1 coupling scheme to multiphase porous media in which solid and fluid motions at the same material point are not identical.

To enforce weak compatibility in the overlapped domain, we introduce Lagrange multipliers for the solid displacement $\boldsymbol{\lambda}_{\boldsymbol{u}} \in \boldsymbol{V}_{\lambda u}$ and fluid pressure $\lambda_p \in V_{\lambda p}$ defined in the spaces of

$$\boldsymbol{V}_{\lambda u} = \{\boldsymbol{\lambda}_{\boldsymbol{u}} : \mathcal{B} \to \mathcal{R}^3 | \boldsymbol{\lambda}_{\boldsymbol{u}} \in [H^1(\mathcal{B})]^3\}, \tag{2.43}$$

$$V_{\lambda p} = \{\lambda_p : \mathcal{B} \to \mathcal{R} | \lambda_p \in [H^1(\mathcal{B})]\}. \tag{2.44}$$

The admissible variations of the Lagrange multipliers belong to $\delta\boldsymbol{\lambda}_{\boldsymbol{u}} \in \boldsymbol{V}_{\lambda u}$ and $\delta\lambda_p \in V_{\lambda p}$. Then, constraints that minimize the discrepancies between the solid displacement fields as well as those between the fluid pressure fields lead to the following compatibility energy functionals

$$\phi[\boldsymbol{\varphi}_{u,n+1}, \boldsymbol{\varphi}_{p,n+1}, \boldsymbol{\lambda}_{\boldsymbol{u},n+1}, \lambda_{p,n+1}]_{n+1} = \phi_{\boldsymbol{u}}[\boldsymbol{\varphi}_{u,n+1}, \boldsymbol{\lambda}_{\boldsymbol{u},n+1}]_{n+1} + \phi_p[\boldsymbol{\varphi}_{p,n+1}, \lambda_{p,n+1}]_{n+1} \tag{2.45}$$

DOI: 10.1002/nme

where

$$\phi_{\boldsymbol{u}}[\boldsymbol{\varphi}_{u,n+1}, \boldsymbol{\lambda}_{\boldsymbol{u},n+1}]_{n+1} = \int_{\mathcal{B}^c} \left[\boldsymbol{\lambda}_{\boldsymbol{u},n+1} \cdot (\overline{\boldsymbol{u}}_{n+1} - \tilde{\boldsymbol{u}}_{n+1}) + \beta l^2 \nabla^{\mathrm{sym}} \boldsymbol{\lambda}_{\boldsymbol{u}} \,:\, (\nabla^{\mathrm{sym}} \overline{\boldsymbol{u}}_{n+1} - \nabla^{\mathrm{sym}} \tilde{\boldsymbol{u}}_{n+1})\right] dV \quad (2.46)$$

$$\phi_p[\boldsymbol{\varphi}_{p,n+1}, \lambda_{p,n+1}]_{n+1} = \int_{\mathcal{B}^c} \left[\lambda_p(\overline{p}_{n+1} - \tilde{p}_{n+1}) + \kappa l^2 \nabla \lambda_{p,n+1} \cdot (\nabla \overline{p}_{n+1} - \nabla \tilde{p}_{n+1})\right] dV. \quad (2.47)$$

Here, $\beta \in [0,1]$ and $\kappa \in [0,1]$ are non-dimensional parameters and l is a scaling factor that has the dimension of length. When both β and κ are zero, the compatibility energy functionals minimize the L_2 norm of the discrepancies between the coarse and fine solution fields. Otherwise, they minimize the H^1 norm of the discrepancies.

Augmenting these compatibility functionals, we now state the incremental energy functional for the Arlequin poromechanics as follows:

$$\begin{aligned} H_{Ar}[\boldsymbol{\varphi}_{u,n+1}, \boldsymbol{\varphi}_{p,n+1}, \boldsymbol{\lambda}_{\boldsymbol{u},n+1}, \lambda_{p,n+1}]_{n+1} = {} & (1-\chi)\overline{H}[\overline{\boldsymbol{u}}_{n+1}, \overline{p}_{n+1}]_{n+1} + \chi \tilde{H}[\tilde{\boldsymbol{u}}_{n+1}, \tilde{p}_{n+1}]_{n+1} \\ & - (1-\chi)\overline{\Omega}[\overline{p}_{n+1}]|_n^{n+1} + \chi \tilde{\Omega}[\tilde{p}_{n+1}]|_n^{n+1} \\ & + \phi[\boldsymbol{\varphi}_{u,n+1}, \boldsymbol{\varphi}_{p,n+1}, \boldsymbol{\lambda}_{\boldsymbol{u},n+1}, \lambda_{p,n+1}]_{n+1}. \end{aligned} \quad (2.48)$$

The saddle point of the incremental Arlequin energy functional (2.48) results in the following set of time-discrete governing equations that give incremental updates of the displacement, pore pressure, and Lagrange multipliers:

$$\begin{aligned} DH_{Ar}[\delta\overline{\boldsymbol{u}}] = {} & \chi \left(\int_{\overline{\mathcal{B}}} \overline{\boldsymbol{\sigma}}'_{n+1} \,:\, \nabla^{\mathrm{sym}} \delta\overline{\boldsymbol{u}} - B\overline{p}_{n+1} \nabla \cdot \ \delta\overline{\boldsymbol{u}} - \overline{\boldsymbol{\gamma}} \delta\overline{\boldsymbol{u}} \ dV - \int_{\partial_t \overline{\mathcal{B}}} \hat{\boldsymbol{t}} \cdot \delta\overline{\boldsymbol{u}} \, d\Gamma \right) \\ & + \int_{\mathcal{B}^c} \left[\boldsymbol{\lambda}_{\boldsymbol{u},n+1} \cdot (\delta\overline{\boldsymbol{u}}) + \beta l^2 \nabla^{\mathrm{sym}} \boldsymbol{\lambda}_{\boldsymbol{u},n+1} \,:\, (\nabla^{\mathrm{sym}} \delta\overline{\boldsymbol{u}})\right] dV = 0, \end{aligned} \quad (2.49)$$

$$\begin{aligned} DH_{Ar}[\delta\tilde{\boldsymbol{u}}] = {} & (1-\chi) \left(\int_{\tilde{\mathcal{B}}} \tilde{\boldsymbol{\sigma}}'_{n+1} \,:\, \nabla^{\mathrm{sym}} \delta\tilde{\boldsymbol{u}} - B\tilde{p}_{n+1} \nabla \cdot \ \delta\tilde{\boldsymbol{u}} - \tilde{\boldsymbol{\gamma}} \delta\tilde{\boldsymbol{u}} \ dV - \int_{\partial_t \tilde{\mathcal{B}}} \hat{\boldsymbol{t}} \cdot \delta\tilde{\boldsymbol{u}} \, d\Gamma \right) \\ & - \int_{\mathcal{B}^c} \left[\boldsymbol{\lambda}_{\boldsymbol{u},n+1} \cdot (\delta\tilde{\boldsymbol{u}}) + \beta l^2 \nabla^{\mathrm{sym}} \boldsymbol{\lambda}_{\boldsymbol{u},n+1} \,:\, (\nabla^{\mathrm{sym}} \delta\tilde{\boldsymbol{u}})\right] dV = 0, \end{aligned} \quad (2.50)$$

$$\begin{aligned} DH_{Ar}[\delta\overline{p}] = {} & \chi \left(\int_{\overline{\mathcal{B}}} \frac{1}{M}(\overline{p}_{n+1} - \overline{p}_n) \ \delta\overline{p} + B\nabla \cdot \ (\overline{\boldsymbol{u}}_{n+1} - \overline{\boldsymbol{u}}_n)\delta\overline{p} \ dV \right. \\ & \left. - \Delta t \int_{\overline{\mathcal{B}}} \nabla \cdot \ \frac{1}{\mu} \boldsymbol{k} \cdot (\nabla \overline{p}_{n+1} - \rho_f \boldsymbol{g}) \delta\overline{p} \ dV - \int_{\partial_q \mathcal{B}} \hat{\boldsymbol{q}} \cdot \overline{\boldsymbol{n}} \ \delta\overline{p} \, d\Gamma \right) \\ & + \int_{\mathcal{B}^c} \left[\lambda_{p,n+1} \delta\overline{p} + \kappa l^2 \nabla \lambda_{p,n+1} \cdot \nabla \delta\overline{p}\right] dV = 0, \end{aligned} \quad (2.51)$$

$$\begin{aligned} DH_{Ar}[\delta\tilde{p}] = {} & (1-\chi) \left(\int_{\tilde{\mathcal{B}}} \frac{1}{M}(\tilde{p}_{n+1} - \tilde{p}_n) \ \delta\tilde{p} + B\nabla \cdot \ (\tilde{\boldsymbol{u}}_{n+1} - \tilde{\boldsymbol{u}}_n)\delta\tilde{p} \ dV \right. \\ & \left. - \Delta t \int_{\tilde{\mathcal{B}}} \nabla \cdot \ \frac{1}{\mu} \boldsymbol{k} \cdot (\nabla \tilde{p}_{n+1} - \rho_f \boldsymbol{g}) \delta\tilde{p} \ dV - \int_{\partial_q \mathcal{B}} \hat{\boldsymbol{q}} \cdot \tilde{\boldsymbol{n}} \ \delta\tilde{p} \, d\Gamma \right) \\ & + \int_{\mathcal{B}^c} \left[\lambda_{p,n+1} \delta\tilde{p} + \kappa l^2 \nabla \lambda_{p,n+1} \cdot (\nabla \delta\tilde{p})\right] dV = 0, \end{aligned} \quad (2.52)$$

$$DH_{Ar}[\delta\boldsymbol{\lambda}_{\boldsymbol{u}}] = \int_{\mathcal{B}^c} \left[\delta\boldsymbol{\lambda}_{\boldsymbol{u}} \cdot (\overline{\boldsymbol{u}}_{n+1} - \tilde{\boldsymbol{u}}_{n+1}) + \beta l^2 \nabla^{\mathrm{sym}} \delta\boldsymbol{\lambda}_{\boldsymbol{u}} \,:\, (\nabla^{\mathrm{sym}} \overline{\boldsymbol{u}}_{n+1} - \nabla^{\mathrm{sym}} \tilde{\boldsymbol{u}}_{n+1})\right] dV = 0, \quad (2.53)$$

$$DH_{Ar}[\delta\lambda_p] = \int_{\mathcal{B}^c} \left[\delta\lambda_p(\overline{p}_{n+1} - \tilde{p}_{n+1}) + \kappa l^2 \nabla \delta\lambda_{p,n+1} \cdot (\nabla \overline{p}_{n+1} - \nabla \tilde{p}_{n+1})\right] dV = 0, \quad (2.54)$$

DOI: 10.1002/nme

where the variations of solid displacement, $(\delta\overline{\boldsymbol{u}}, \delta\tilde{\boldsymbol{u}})$, fluid pressure $(\delta\overline{p}, \delta\tilde{p})$, and Lagrange multipliers $(\delta\overline{\boldsymbol{\lambda}_{\boldsymbol{u}}}, \delta\widetilde{\lambda_p})$ are arbitrary fields.

2.5. Galerkin and matrix forms

We now apply the standard Galerkin method to discretize (2.49)–(2.54) in space. In doing so, we employ equal-order spatial discretization for the solid displacement and fluid pressure variables for both the fine and coarse domains [52]. The rationale behind employing equal-order mixed finite elements instead of inf–sup stable higher-order elements is to reduce the minimum number of finite-dimensional spaces required for the Arlequin method from 4 to 2. This reduction significantly simplifies the formulation.

Let the Lagrange multiplier for solid displacement $\boldsymbol{\lambda}_{\boldsymbol{u}}(\boldsymbol{x})$ be spanned by the same set of basis functions that interpolate the coarse displacement field. Similarly, let the Lagrange multiplier for the fluid pressure $\lambda_p(\boldsymbol{x})$ be also spanned by the same set of basis functions that interpolate by the coarse fluid pressure field. This arrangement is motivated by the finding of Guidault and Belytschko [66] that the use of the same basis functions for interpolating the Lagrange multiplier and fine displacement field would lead to severe locking. This treatment also simplifies the setup of the boundary value problem, because there is no need to generate extra meshes for the Lagrange multiplier. Thus, we have

$$
\begin{aligned}
\overline{\boldsymbol{u}}^h(\boldsymbol{x}) &= \overline{\boldsymbol{N}}_A(\boldsymbol{x})\overline{\boldsymbol{U}}_A \in V^h_{\overline{\boldsymbol{u}}}, \quad \overline{\delta\boldsymbol{u}}^h(\boldsymbol{x}) = \overline{\boldsymbol{N}}_B(\boldsymbol{x})\delta\overline{\boldsymbol{U}}_B \in V^h_{\overline{\boldsymbol{u}}},\\
\tilde{\boldsymbol{u}}^h(\boldsymbol{x}) &= \tilde{\boldsymbol{N}}_a(\boldsymbol{x})\tilde{\boldsymbol{U}}_a \in V^h_{\tilde{\boldsymbol{u}}}, \quad \widetilde{\delta\boldsymbol{u}}^h(\boldsymbol{x}) = \tilde{\boldsymbol{N}}_b(\boldsymbol{x})\delta\tilde{\boldsymbol{U}}_b \in V^h_{\tilde{\boldsymbol{u}}},\\
\overline{p}^h(\boldsymbol{x}) &= \overline{N}_A(\boldsymbol{x})\overline{P}_A \in V^h_{\overline{p}}, \quad \overline{\delta p}^h(\boldsymbol{x}) = \overline{N}_B(\boldsymbol{x})\delta\overline{P}_B \in V^h_{\overline{p}},\\
\tilde{p}^h(\boldsymbol{x}) &= \tilde{N}_a(\boldsymbol{x})\tilde{P}_b \in V^h_{\tilde{p}}, \quad \widetilde{\delta p}^h(\boldsymbol{x}) = \tilde{N}_b(\boldsymbol{x})\delta\tilde{P}_b \in V^h_{\tilde{p}},\\
\boldsymbol{\lambda}^h_{\boldsymbol{u}}(\boldsymbol{x}) &= \overline{\boldsymbol{N}}_A(\boldsymbol{x})\boldsymbol{\Lambda}_A \in V^h_{\boldsymbol{\lambda}_{\boldsymbol{u}}}, \quad \delta\boldsymbol{\lambda}^h_{\boldsymbol{u}}(\boldsymbol{x}) = \overline{\boldsymbol{N}}_B(\boldsymbol{x})\delta\boldsymbol{\Lambda}_B \in V^h_{\boldsymbol{\lambda}_{\boldsymbol{u}}},\\
\lambda^h_p(\boldsymbol{x}) &= \overline{N}_A(\boldsymbol{x})\Xi_A \in V^h_{\lambda_p}, \quad \delta\lambda^h_p(\boldsymbol{x}) = \overline{N}_B(\boldsymbol{x})\delta\Xi_B \in V^h_{\lambda_p},
\end{aligned}
\tag{2.55}
$$

where $(\overline{N}_A, \overline{N}_B)$ are the basis functions for the interpolated solutions and admissible variations of the coarse displacement and pore pressure, whereas $(\tilde{N}_a, \tilde{N}_b)$ are the basis functions for the interpolated solutions and admissible variations of the fine displacement and pore pressure. Also, $(\overline{N}_a, \overline{N}_b)$ are the basis functions for the Lagrange multipliers, which are the same as those for the coarse displacement and pore pressure except that they are confined in the overlapped domain. In addition, $V^h_{\overline{\boldsymbol{u}}} \subset V_{\overline{\boldsymbol{u}}}$, $V^h_{\tilde{\boldsymbol{u}}} \subset V_{\tilde{\boldsymbol{u}}}$, $V^h_{\overline{p}} \subset V_{\overline{p}}$, $V^h_{\tilde{p}} \subset V_{\tilde{p}}$, $V^h_{\boldsymbol{\lambda}_{\boldsymbol{u}}} \subset V_{\boldsymbol{\lambda}_{\boldsymbol{u}}}$, and $V^h_{\lambda_p} \subset V_{\lambda_p}$ are finite-dimensional subspaces spanned by the corresponding interpolation functions.

We now develop the matrix form of the problem. Following the standard finite element procedure, we first insert the interpolated solutions and variations in (2.55) into (2.49)–(2.54), and then eliminate the nodal arbitrary variables for the trial functions. This leads to the following matrix form,

$$
\begin{bmatrix}
\overline{\boldsymbol{K}} & \boldsymbol{0} & \overline{\boldsymbol{G}}^{\mathrm{T}} & \boldsymbol{0} & \overline{\boldsymbol{C}}_u^{\mathrm{T}} & \boldsymbol{0}\\
\boldsymbol{0} & \tilde{\boldsymbol{K}} & \boldsymbol{0} & \tilde{\boldsymbol{G}}^{\mathrm{T}} & -\tilde{\boldsymbol{C}}_u^{\mathrm{T}} & \boldsymbol{0}\\
\overline{\boldsymbol{G}} & \boldsymbol{0} & \overline{\boldsymbol{\Theta}} & \boldsymbol{0} & \boldsymbol{0} & \overline{\boldsymbol{C}}_p^{\mathrm{T}}\\
\boldsymbol{0} & \tilde{\boldsymbol{G}} & \boldsymbol{0} & \tilde{\boldsymbol{\Theta}} & \boldsymbol{0} & -\tilde{\boldsymbol{C}}_p^{\mathrm{T}}\\
\overline{\boldsymbol{C}}_u & -\tilde{\boldsymbol{C}}_u & \boldsymbol{0} & \boldsymbol{0} & \boldsymbol{0} & \boldsymbol{0}\\
\boldsymbol{0} & \boldsymbol{0} & \overline{\boldsymbol{C}}_p & -\tilde{\boldsymbol{C}}_p & \boldsymbol{0} & \boldsymbol{0}
\end{bmatrix}
\begin{bmatrix}
\Delta\overline{\boldsymbol{U}}\\ \Delta\tilde{\boldsymbol{U}}\\ \Delta\overline{\boldsymbol{P}}\\ \Delta\tilde{\boldsymbol{P}}\\ \Delta\boldsymbol{\Lambda}_U\\ \Delta\boldsymbol{\Lambda}_P
\end{bmatrix}
= -
\begin{bmatrix}
\boldsymbol{R}_{\overline{\boldsymbol{u}}}\\ \boldsymbol{R}_{\tilde{\boldsymbol{u}}}\\ \boldsymbol{R}_{\overline{p}}\\ \boldsymbol{R}_{\tilde{p}}\\ \boldsymbol{R}_{\boldsymbol{\lambda}_{\boldsymbol{u}}}\\ \boldsymbol{R}_{\lambda_p}
\end{bmatrix},
\tag{2.56}
$$

where $\Delta\overline{\boldsymbol{U}}, \Delta\tilde{\boldsymbol{U}}, \Delta\overline{\boldsymbol{P}}, \Delta\tilde{\boldsymbol{P}}, \Delta\boldsymbol{\Lambda}_U, \Delta\boldsymbol{\Lambda}_P$ are the solution increments during iterations. The residual vectors in the right hand side are given by:

$$
\begin{aligned}
\boldsymbol{R}_{\overline{\boldsymbol{u}}} = \chi \left(\int_{\overline{\mathcal{B}}} \overline{\boldsymbol{B}}^{\mathrm{T}} \cdot (\overline{\boldsymbol{\sigma}}'_{n+1} - B\boldsymbol{I}\overline{p}_{n+1}) - \overline{\boldsymbol{N}}^{\mathrm{T}}\boldsymbol{\gamma} \; dV - \int_{\partial_{\boldsymbol{T}}\overline{\mathcal{B}}} \overline{\boldsymbol{N}}^{\mathrm{T}}\hat{\boldsymbol{t}}\, d\Gamma \right)\\
+ \int_{\mathcal{B}^c} \left[\overline{\boldsymbol{N}}^{\mathrm{T}}\boldsymbol{\lambda}_{\boldsymbol{u},n+1} + \beta l^2 \overline{\boldsymbol{B}}^{\mathrm{T}}\boldsymbol{\lambda}_{\boldsymbol{u},n+1} \right] dV = 0,
\end{aligned}
\tag{2.57}
$$

DOI: 10.1002/nme

$$\begin{aligned}\boldsymbol{R}_{\tilde{u}} = (1-\chi)\left(\int_{\tilde{\mathcal{B}}} \tilde{\boldsymbol{B}}^{\mathrm{T}} \cdot (\tilde{\boldsymbol{\sigma}}'_{n+1} - B\boldsymbol{I}\tilde{p}_{n+1}) - \tilde{\boldsymbol{N}}^{\mathrm{T}}\boldsymbol{\gamma}\ dV - \int_{\partial_T\tilde{\mathcal{B}}} \tilde{\boldsymbol{N}}^{\mathrm{T}}\hat{\boldsymbol{t}}\, d\Gamma\right) \\ - \int_{\mathcal{B}^c}\left[\tilde{\boldsymbol{N}}^{\mathrm{T}}\boldsymbol{\lambda}_{\boldsymbol{u},n+1} + \beta l^2 \tilde{\boldsymbol{B}}^{\mathrm{T}}\boldsymbol{\lambda}_{\boldsymbol{u},n+1}\right] dV = 0,\end{aligned} \tag{2.58}$$

$$\begin{aligned}\boldsymbol{R}_{\overline{p}} = \chi\left(\int_{\overline{\mathcal{B}}} \overline{\boldsymbol{N}}^{\mathrm{T}}\frac{1}{M}(\overline{p}_{n+1} - \overline{p}_n) + \overline{\boldsymbol{N}}^{\mathrm{T}} B\nabla\cdot\ (\overline{\boldsymbol{u}}_{n+1} - \overline{\boldsymbol{u}}_n)\ dV \right. \\ \left. - \Delta t\int_{\overline{\mathcal{B}}} \nabla\overline{N}^{\mathrm{T}}\cdot\frac{1}{\mu}\boldsymbol{k}(\nabla\overline{p}_{n+1} - \rho_f\boldsymbol{g})\ dV - \Delta t\int_{\partial_q\overline{\mathcal{B}}}\overline{N}^{\mathrm{T}}\boldsymbol{q}\ d\Gamma\right) \\ + \int_{\mathcal{B}^c}\left[\overline{N}^{\mathrm{T}}\boldsymbol{\lambda}_{p,n+1} + \nabla\overline{N}^{\mathrm{T}}\kappa l^2\boldsymbol{k}\nabla\boldsymbol{\lambda}_{p,n+1}\right] dV = 0,\end{aligned} \tag{2.59}$$

$$\begin{aligned}\boldsymbol{R}_{\tilde{p}} = (1-\chi)\left(\int_{\tilde{\mathcal{B}}} \tilde{\boldsymbol{N}}^{\mathrm{T}}\frac{1}{M}(\tilde{p}_{n+1} - \tilde{p}_n) + \tilde{\boldsymbol{N}}^{\mathrm{T}} B\nabla\cdot\ (\tilde{\boldsymbol{u}}_{n+1} - \tilde{\boldsymbol{u}}_n)\ dV \right. \\ \left. - \Delta t\int_{\tilde{\mathcal{B}}} \nabla\tilde{N}^{\mathrm{T}}\cdot\frac{1}{\mu}\boldsymbol{k}(\nabla\tilde{p}_{n+1} - \rho_f\boldsymbol{g})\ dV - \Delta t\int_{\partial_q\overline{\mathcal{B}}}\tilde{N}^{\mathrm{T}}\boldsymbol{q}\ d\Gamma\right) \\ - \int_{\mathcal{B}^c}\left[\tilde{N}^{\mathrm{T}}\boldsymbol{\lambda}_{p,n+1} + \nabla\tilde{N}^{\mathrm{T}}\kappa l^2\nabla\boldsymbol{\lambda}_{p,n+1}\right] dV = 0,\end{aligned} \tag{2.60}$$

$$\boldsymbol{R}_{\lambda_u} = \int_{\mathcal{B}^c}\left[\overline{N}^{\mathrm{T}}\cdot(\overline{\boldsymbol{u}}_{n+1} - \tilde{\boldsymbol{u}}_{n+1}) + \beta l^2\overline{B}^{\mathrm{T}}\cdot(\nabla^{\mathrm{sym}}\overline{\boldsymbol{u}}_{n+1} - \nabla^{\mathrm{sym}}\tilde{\boldsymbol{u}}_{n+1})\right] dV = 0, \tag{2.61}$$

$$\boldsymbol{R}_{\lambda_p} = \int_{\mathcal{B}^c}\left[\overline{N}^{\mathrm{T}}(\overline{p}_{n+1} - \tilde{p}_{n+1}) + \kappa l^2\nabla\overline{N}^{\mathrm{T}}(\nabla\overline{p}_{n+1} - \nabla\tilde{p}_{n+1})\right] dV = 0, \tag{2.62}$$

where $\overline{\boldsymbol{N}} = [\overline{N}_1, \overline{N}_2, \ldots, \overline{N}_{n\overline{u}}]$ and $\tilde{\boldsymbol{N}} = [\tilde{N}_1, \tilde{N}_2, \ldots, \tilde{N}_{n\tilde{u}}]$ are the $\boldsymbol{N}$ matrices for the coarse and fine domains where the basis function are stored in the matrix form ($n\overline{u}$ and $n\tilde{u}$ are the numbers of nodes in the coarse and fine domains). Also, $\overline{\boldsymbol{B}} = [\overline{\boldsymbol{B}}_1, \overline{\boldsymbol{B}}_2, \ldots, \overline{\boldsymbol{B}}_{n\overline{u}}]$ and $\tilde{\boldsymbol{B}} = [\tilde{\boldsymbol{B}}_1, \tilde{\boldsymbol{B}}_2, \ldots, \tilde{\boldsymbol{B}}_{n\tilde{u}}]$ are the $\boldsymbol{B}$ matrices for the coarse and fine domains, given by

$$\overline{\boldsymbol{B}}_A = \begin{bmatrix} \overline{N}_{A,1} & 0 & 0 \\ 0 & \overline{N}_{A,2} & 0 \\ 0 & 0 & \overline{N}_{A,3} \\ \overline{N}_{A,2} & \overline{N}_{A,1} & 0 \\ 0 & \overline{N}_{A,3} & \overline{N}_{A,2} \\ \overline{N}_{A,1} & 0 & \overline{N}_{A,3} \end{bmatrix};\ \tilde{\boldsymbol{B}}_a = \begin{bmatrix} \tilde{N}_{a,1} & 0 & 0 \\ 0 & \tilde{N}_{a,2} & 0 \\ 0 & 0 & \tilde{N}_{a,3} \\ \tilde{N}_{a,2} & \tilde{N}_{a,1} & 0 \\ 0 & \tilde{N}_{a,3} & \tilde{N}_{a,2} \\ \tilde{N}_{a,1} & 0 & \tilde{N}_{a,3} \end{bmatrix} \tag{2.63}$$

The submatrices of the tangent (Jacobian) matrix in (2.56) are obtained as follows. First, the tangential stiffness matrices of the solid skeleton in the coarse and fine domains are given by

$$\overline{\boldsymbol{K}} = \frac{\partial\boldsymbol{R}_{\overline{u}}}{\partial\overline{\boldsymbol{U}}} = \int_{\overline{\mathcal{B}}}\chi\overline{\boldsymbol{B}}^{\mathrm{T}}\overline{\mathbb{D}}\,\overline{\boldsymbol{B}}\ dV, \quad \tilde{\boldsymbol{K}} = \frac{\partial\boldsymbol{R}_{\tilde{u}}}{\partial\tilde{\boldsymbol{U}}} = \int_{\tilde{\mathcal{B}}}(1-\chi)\tilde{\boldsymbol{B}}^{\mathrm{T}}\tilde{\mathbb{D}}\,\tilde{\boldsymbol{B}}\ dV, \tag{2.64}$$

where $\overline{\mathbb{D}}$ and $\tilde{\mathbb{D}}$ are the tangential stiffness tensors defined in (2.11), corresponding to the models used in the coarse and fine domains. Once again, we emphasize that while these two models capture the same physical processes in the overlapped domain, but the choices of the mesh size, constitutive laws and basis functions used to interpolate the solution can be different.

DOI: 10.1002/nme

The two non-zero components of the 2-by-2 block at the center of the Jacobian matrix are the hydraulic components that consist of two terms—one for the fluid mass changes due to local changes of pore pressure and another for the fluid diffusion. For instance, if the effective permeability and Biot's modulus are constant, then the two matrices read,

$$\overline{\boldsymbol{\Theta}} = \frac{\partial \boldsymbol{R}_{\overline{p}}}{\partial \overline{\boldsymbol{P}}} = -\Delta t \overline{\boldsymbol{E}} - \overline{\boldsymbol{\Phi}}, \quad \tilde{\boldsymbol{\Theta}} = \frac{\partial \boldsymbol{R}_{\tilde{p}}}{\partial \tilde{\boldsymbol{P}}} = -\Delta t \tilde{\boldsymbol{E}} - \tilde{\boldsymbol{\Phi}}, \tag{2.65}$$

where

$$\overline{\boldsymbol{E}} = \int_{\overline{\mathcal{B}}} \chi \nabla \overline{\boldsymbol{N}}^{\mathrm{T}} \frac{1}{\mu} \boldsymbol{k} \nabla \overline{\boldsymbol{N}} \, dV, \quad \tilde{\boldsymbol{E}} = \int_{\tilde{\mathcal{B}}} (1-\chi) \nabla \tilde{\boldsymbol{N}}^{\mathrm{T}} \frac{k}{\mu} \nabla \tilde{\boldsymbol{N}} \, dV, \tag{2.66}$$

$$\overline{\boldsymbol{\Phi}} = \int_{\overline{\mathcal{B}}} \chi \overline{\boldsymbol{N}}^{\mathrm{T}} \frac{1}{M} \overline{\boldsymbol{N}} \, dV, \quad \tilde{\boldsymbol{\Phi}} = \int_{\tilde{\mathcal{B}}} (1-\chi) \tilde{\boldsymbol{N}}^{\mathrm{T}} \frac{1}{M} \tilde{\boldsymbol{N}} \, dV. \tag{2.67}$$

The coupling matrices that represent the hydro-mechanical coupling are defined as

$$\overline{\boldsymbol{G}} = \frac{\partial \boldsymbol{R}_{\overline{p}}}{\partial \overline{\boldsymbol{U}}} = \int_{\overline{\mathcal{B}}} \overline{\boldsymbol{N}}^{\mathrm{T}} \overline{\boldsymbol{b}} \, dV, \quad \tilde{\boldsymbol{G}} = \frac{\partial \boldsymbol{R}_{\tilde{p}}}{\partial \tilde{\boldsymbol{U}}} = \int_{\tilde{\mathcal{B}}} \tilde{\boldsymbol{N}}^{\mathrm{T}} \tilde{\boldsymbol{b}} \, dV, \tag{2.68}$$

where $\overline{\boldsymbol{b}} = \overline{\boldsymbol{B}} \cdot \mathbf{1}$ and $\tilde{\boldsymbol{b}} = \tilde{\boldsymbol{B}} \cdot \mathbf{1}$ with $\mathbf{1} = [1\ 1\ 1\ 0\ 0\ 0]^{\mathrm{T}}$ B, again, is Biot's coefficient. The coupling matrices that enforce the compatibility of the solid displacement are defined as

$$\overline{\boldsymbol{C}}_u = \frac{\partial \boldsymbol{R}_{\lambda_u}}{\partial \overline{\boldsymbol{U}}} = \int_{\mathcal{B}^c} \overline{\boldsymbol{N}}^{\mathrm{T}} \overline{\boldsymbol{N}} + \beta l^2 \overline{\boldsymbol{B}}^{\mathrm{T}} \overline{\boldsymbol{B}} \, dV, \quad \tilde{\boldsymbol{C}}_u = \frac{\partial \boldsymbol{R}_{\lambda_u}}{\partial \tilde{\boldsymbol{U}}} = \int_{\mathcal{B}^c} \overline{\boldsymbol{N}}^{\mathrm{T}} \tilde{\boldsymbol{N}} + \beta l^2 \overline{\boldsymbol{B}}^{\mathrm{T}} \tilde{\boldsymbol{B}} \, dV. \tag{2.69}$$

Lastly, the coupling matrices that enforce the compatibility of the fluid pressure are defined as

$$\overline{\boldsymbol{C}}_p = \frac{\partial \boldsymbol{R}_{\lambda_p}}{\partial \tilde{\boldsymbol{P}}} = \int_{\mathcal{B}^c} \overline{\boldsymbol{N}}^{\mathrm{T}} \overline{\boldsymbol{N}} + \kappa l^2 \nabla \overline{\boldsymbol{N}}^{\mathrm{T}} \nabla \overline{\boldsymbol{N}} \, dV, \quad \tilde{\boldsymbol{C}}_p = \frac{\partial \boldsymbol{R}_{\lambda_p}}{\partial \tilde{\boldsymbol{P}}} = \int_{\mathcal{B}^c} \overline{\boldsymbol{N}}^{\mathrm{T}} \tilde{\boldsymbol{N}} + \kappa l^2 \nabla \overline{\boldsymbol{N}}^{\mathrm{T}} \nabla \tilde{\boldsymbol{N}} \, dV. \tag{2.70}$$

Because we use the basis function of the coarse solution field to interpolate the Lagrange multipliers, the numerical integration of all block matrices—except $\tilde{\boldsymbol{C}}_u$ and $\tilde{\boldsymbol{C}}_p$—can be performed via standard Gauss quadrature rules. The calculation of $\tilde{\boldsymbol{C}}_u$ and $\tilde{\boldsymbol{C}}_p$ can be more complicated, as the $\tilde{\boldsymbol{C}}_u$ and $\tilde{\boldsymbol{C}}_p$ matrices consist of expressions in terms of both the coarse and fine basis functions. Here, we numerically integrate the integrand expressed in the isoparametric (natural) coordinates of the fine mesh and perform the standard full integration over the fine mesh elements. This approach requires one to evaluate the coarse basis function at non-standard locations in the isoparametric coordinates of the fine mesh. β and κ are dimensionless parameters that control the weight of the gradient term in the norms used to measure the discrepancies. If $\beta = \kappa = 0$, then the L_2 error of displacement and pore pressure is minimized. l is a parameter which makes the constraint dimensionless. Our analysis indicates that introducing the gradient term in the compatibility functionals may improve numerical stability. This result is explained further in the next section.

We note that this matrix system may be ill-conditioned for two reasons. One reason is the introduction of Lagrange multipliers for domain coupling [33], and another is the coupling between solid deformation and fluid flow [68,69]. Therefore, making the use of an iterative solver for this linear system requires a preconditioning strategy that effectively handles these two sources of ill-conditioning. White et al. [70] have recently developed a framework for block-partitioned solvers for coupled poromechanics problems, whereas Sun and Mota [33] present a block solver for overlapped domain problems in solid mechanics problem. In the former case, the condition number of the matrix system of the poromechanics problem may increase significantly when a smaller time step is used. While we use direct solvers in this work and hence the usage of preconditioner is less critical, the usage of direct solvers is rarely a practical option for large-scale problems due to the relatively high computational demands and lower speed of the direct solver. As a result, a proper design for preconditioner

DOI: 10.1002/nme

for the Arlequin poromechanics problems is an important future work, especially for solving large-scale problems that require an efficient iterative solver. The design of such a preconditioner is outside the scope of this work but will be considered in future studies.

3. NUMERICAL STABILITY

The objective of this section is to derive a numerical test that examines the spatial stability of the Arlequin poromechanics formulation. A necessary (but not sufficient) condition for the convergence of an implicit solution method for nonlinear problems is the stability of the linearized system of equations such as (2.56). For single-field finite elements, well-posedness and numerical stability of an incremental update can be guaranteed if the tangent operator is both coercive and consistent. However, a tangent operator in mixed finite elements, such as those for solving multiphysical problems like poromechanics, may lack coercivity. In such cases, one must ensure that at least one diagonal block of the block-partitioned Jacobian matrix is positive definite [71,72].

Mixed finite elements for constrained multi-field problems should satisfy the inf–sup condition to maintain the spatial stability of numerical solutions [71–74]. When the inf–sup condition is not satisfied, the kernel space of the coupling operator(s) in the governing equation is spanned by non-trivial basis, which in turn gives rise to spurious (physically meaningless) oscillations in the numerical solutions. In poromechanics, it is well known that the inf–sup condition arises when the pore fluid imposes an incompressibility constraint in the solid deformation—which is common especially in the early stages of loading. As such, mixed finite elements that employ equal-order interpolations for the displacement and pore pressure fields may result in spurious oscillations in the pore pressure field, see [1,51,52,75–78] for example.

The introduction of the Arlequin method for poromechanics problems complicates the analysis of spatial stability because it adds additional type of constraints. Hence, multiple Lagrange multipliers are used in the overlapping domains to enforce compatibility for both the solid and fluid constituents. As shown in (2.56), the Arlequin method embeds the hydro-mechanical coupling blocks into another block system that incorporates constraints enforcing domain compatibility. Previous studies have analyzed the inf–sup condition of the Arlequin method for single-physics solid mechanics problems [28,33]. Furthermore, Jamond and Ben Dhia [38] have analyzed, within the Arlequin framework, critical zones for an incompressible medium modeled via a two-field mixed formulation. To avoid redundancy in the overlapped domain that may lead to pathological results, they weakly enforce the incompressibility for only one of the two super-imposed models. Interestingly, the poromechanics theory may also lead to a two-field $\boldsymbol{u}/p$ mixed finite element formulation and a similar block matrix system that resembles the incompressible elasticity counterpart at the undrained limit. However, because the flow of the pore fluid is related to the gradient of pore pressure, the pore pressure field must exist in all sub-domains to capture the hydro-mechanical coupling effects. As a result, the analysis of spatial stability of the Arlequin method for poromechanics requires a further endeavor and examination. In particular, this analysis requires us to tackle the spatial stability of the Arlequin coupling model whereby two primary fields are both constrained, which has not yet been attempted to the best of the authors' knowledge. Our new contribution in this work is to address the inf–sup condition that arises from the multiscale coupling of the mixed Arlequin poromechanics model. In doing so, we ensure the spatial stability in non-overlapped domains by using the polynomial projection stabilization procedure, which has been successfully applied to various constrained problems including poromechanics [45,51,52,75,77]. In essence, the stabilization procedure augments the following additional term to the incremental energy functional $H_{Ar}[\boldsymbol{\varphi}_{u,n+1}, \boldsymbol{\varphi}_{p,n+1}, \boldsymbol{\lambda}_{\boldsymbol{u},n+1}, \boldsymbol{\lambda}_{p,n+1}]_{n+1}$ in (2.48)

$$W^{\text{stab}}(\Delta\overline{p}^h, \Delta\tilde{p}^h) = \frac{1}{2}\int_{\mathcal{B}} \chi\alpha(\Delta\overline{p} - \Pi\Delta\tilde{p})^2 \, dV + \frac{1}{2}\int_{\mathcal{B}} (1-\chi)\alpha(\Delta\tilde{p} - \Pi\Delta\tilde{p})^2 \, dV, \tag{3.1}$$

where $\Pi(\cdot)$ denotes a projection operator that project the interpolated pore pressure field onto an element-wise constant, and α is the stabilization parameter whose optimal value depends on both the effective diffusivity and the element size.

Lastly, we emphasize that it is also possible to couple finite elements that are individually inf–sup stable within the Arlequin framework. However, this approach requires selecting multiple finite

DOI: 10.1002/nme

dimensional spaces for the coarse and fine displacements, pore pressures, and Lagrangian multipliers. Consequently, more elaborated efforts must be spent for the implementation, without any guarantee that the coupling of two inf–sup stable mixed finite elements through Lagrangian multipliers remains stable in the overlapped domain.

3.1. Twofold inf–sup condition for Arlequin poromechanics problems

Here, we show that one can analyze the spatial stability of the Arlequin poromechanics problem by checking the twofold inf–sup condition, the inf–sup condition arising from a twofold saddle point problem. Howell and Walkington [79] derived this condition, and Sun [52] and Choo and Borja [77] developed stabilization methods for this condition in the contexts of thermo-poro-mechanics and two-scale poromechanics, respectively.

The key idea of this work is to analyze the multi-field Arlequin problem with the product spaces equipped with weighted product norms. For instance, one may group the solution of the system of equations in (2.56) in the following three product spaces: $\boldsymbol{V}^h_{\overline{\boldsymbol{u}}} \times \boldsymbol{V}^h_{\tilde{\boldsymbol{u}}}$, $\boldsymbol{V}^h_{\overline{p}} \times \boldsymbol{V}^h_{\tilde{p}}$, and $\boldsymbol{V}^h_{\lambda_{\boldsymbol{u}}} \times \boldsymbol{V}^h_{\lambda_p}$. The corresponding matrix form therefore reads

$$\begin{bmatrix} \mathbb{K} & \mathbb{G}^{\mathrm{T}} & \mathbb{C}_{\boldsymbol{u}}^{\mathrm{T}} \\ \mathbb{G} & \mathbb{D} & \mathbb{C}_p^{\mathrm{T}} \\ \mathbb{C}_{\boldsymbol{u}} & \mathbb{C}_p & \mathbf{0} \end{bmatrix} \begin{bmatrix} \Delta\hat{\boldsymbol{U}} \\ \Delta\hat{\boldsymbol{P}} \\ \Delta\boldsymbol{\Lambda} \end{bmatrix} = - \begin{bmatrix} \boldsymbol{R}_{\boldsymbol{u}} \\ \boldsymbol{R}_p \\ \boldsymbol{R}_\lambda \end{bmatrix}, \tag{3.2}$$

where the block matrices in (3.2) are given by

$$\mathbb{K} = \begin{bmatrix} \overline{\boldsymbol{K}} & \mathbf{0} \\ \mathbf{0} & \tilde{\boldsymbol{K}} \end{bmatrix}, \quad \mathbb{D} = \begin{bmatrix} \overline{\boldsymbol{\Theta}} & \mathbf{0} \\ \mathbf{0} & \tilde{\boldsymbol{\Theta}} \end{bmatrix}, \mathbb{G} = \begin{bmatrix} \overline{\boldsymbol{G}} & \mathbf{0} \\ \mathbf{0} & \tilde{\boldsymbol{G}} \end{bmatrix}, \mathbb{C}_{\boldsymbol{u}} = \begin{bmatrix} \overline{\boldsymbol{C}}_{\boldsymbol{u}} & -\tilde{\boldsymbol{C}}_{\boldsymbol{u}} \\ \mathbf{0} & \mathbf{0} \end{bmatrix}, \mathbb{C}_p = \begin{bmatrix} \mathbf{0} & \mathbf{0} \\ \overline{\boldsymbol{C}}_p & -\tilde{\boldsymbol{C}}_p \end{bmatrix}, \tag{3.3}$$

and $\Delta\hat{\boldsymbol{U}}$, $\Delta\hat{\boldsymbol{P}}$, and $\boldsymbol{\Delta\Lambda}$ are the column vectors of the solution fields, that is,

$$\Delta\hat{\boldsymbol{U}} = \begin{bmatrix} \Delta\overline{\boldsymbol{U}} \\ \Delta\tilde{\boldsymbol{U}} \end{bmatrix}, \quad \Delta\hat{\boldsymbol{P}} = \begin{bmatrix} \Delta\overline{\boldsymbol{P}} \\ \Delta\tilde{\boldsymbol{P}} \end{bmatrix}, \Delta\boldsymbol{\Lambda} = \begin{bmatrix} \Delta\boldsymbol{\Lambda}_{\boldsymbol{U}} \\ \Delta\boldsymbol{\Lambda}_{\boldsymbol{P}} \end{bmatrix}. \tag{3.4}$$

The product spaces of the solutions for the combined solid displacement, pore pressure, and Lagrange multipliers therefore read

$$\hat{\boldsymbol{u}} \in \boldsymbol{V}^h_{\hat{\boldsymbol{u}}} = \boldsymbol{V}^h_{\overline{\boldsymbol{u}}} \times \boldsymbol{V}^h_{\tilde{\boldsymbol{u}}}, \quad \hat{\boldsymbol{p}} \in \boldsymbol{V}^h_{\hat{\boldsymbol{p}}} = \boldsymbol{V}^h_{\overline{p}} \times \boldsymbol{V}^h_{\tilde{p}}, \quad \boldsymbol{\lambda} \in \boldsymbol{V}_\lambda = \boldsymbol{V}^h_{\lambda_{\boldsymbol{u}}} \times \boldsymbol{V}^h_{\lambda_p}, \tag{3.5}$$

which are equipped with the following product norms,

$$||\hat{\boldsymbol{u}}||_{V_{\hat{\boldsymbol{u}}}} = \sqrt{||\overline{\boldsymbol{u}}||_2 + ||\tilde{\boldsymbol{u}}||_2} \;;\; ||\hat{\boldsymbol{p}}||_{V_{\hat{\boldsymbol{p}}}} = \sqrt{||\overline{\boldsymbol{p}}||_2 + ||\tilde{\boldsymbol{p}}||_2} \;;\; ||\boldsymbol{\lambda}||_W = \sqrt{w_u||\boldsymbol{\lambda}_{\boldsymbol{u}}||_2 + w_p||\boldsymbol{\lambda}_p||_2}, \tag{3.6}$$

where $||\cdot||_2$ denotes the L_2 norm, and w_u and w_p are the weighting functions for Lagrange multipliers. Following Auricchio et al. [80], we further condense the system of equations as a problem coupled by a composite coupling operator $\mathbb{B}$, that is,

$$\begin{bmatrix} \mathbb{A} & \mathbb{B}^{\mathrm{T}} \\ \mathbb{B} & \mathbf{0} \end{bmatrix} \begin{bmatrix} \boldsymbol{x} \\ \boldsymbol{y} \end{bmatrix} = \begin{bmatrix} \boldsymbol{f} \\ \boldsymbol{g} \end{bmatrix} \tag{3.7}$$

where:

$$\mathbb{A} = \begin{bmatrix} \mathbb{K} & \mathbb{G}^{\mathrm{T}} \\ \mathbb{G} & \mathbb{D} \end{bmatrix}, \quad \mathbb{B} = \begin{bmatrix} \mathbb{C}_u & \mathbb{C}_p \end{bmatrix}, \quad \boldsymbol{x} = \begin{bmatrix} \Delta\hat{\boldsymbol{U}} \\ \Delta\hat{\boldsymbol{P}} \end{bmatrix}, \quad \boldsymbol{y} = \Delta\boldsymbol{\Lambda}. \tag{3.8}$$

DOI: 10.1002/nme

The kernel of coupling operator is made by ($\Delta\hat{\boldsymbol{U}},\ \Delta\hat{\boldsymbol{P}}$) such that:

$$\mathbb{C}_u\Delta\hat{\boldsymbol{U}} + \mathbb{C}_p\Delta\hat{\boldsymbol{P}} = \boldsymbol{0}. \tag{3.9}$$

The key step to simplify the analysis is to take advantage of the fact that the spaces $\boldsymbol{V}_{\boldsymbol{u}}^h$, $\boldsymbol{V}_p^h$, and $\boldsymbol{V}_\lambda$ are all finite dimensional and spanned by the basis function (cf. [74,80]). This fact allows us to construct a bijective map from the finite dimensional spaces $\boldsymbol{V}_{\boldsymbol{u}}^h$, $\boldsymbol{V}_p^h$, and $\boldsymbol{V}_\lambda$ onto the Euclidean space of the nodal solution. Let N_u, N_p, and N_λ be the dimensions of the nodal solution $\hat{\boldsymbol{U}} \in \mathbb{R}^{N_u}$, $\hat{\boldsymbol{P}} \in \mathbb{R}^{N_p}$, and $\boldsymbol{\Lambda} \in \mathbb{R}^{N_\lambda}$. Then, we can express the twofold inf–sup condition as follows:

Twofold inf–sup condition. *There exists a positive constant β_s, independent of the mesh size, such that:*

$$\sup_{(\hat{\boldsymbol{U}}\in\mathbb{R}^{N_u}\setminus\{\boldsymbol{0}\},\hat{\boldsymbol{P}}\in\mathbb{R}^{N_p}\setminus\{\boldsymbol{0}\},)} \frac{\boldsymbol{\Lambda}^{\mathrm{T}}\mathbb{C}_u\hat{\boldsymbol{U}} + \boldsymbol{\Lambda}^{\mathrm{T}}\mathbb{C}_p\hat{\boldsymbol{P}}}{||\hat{\boldsymbol{P}}||_{\boldsymbol{V}_P} + ||\hat{\boldsymbol{U}}||_{\boldsymbol{V}_U}} \geqslant \beta_s \ \forall\ ||\boldsymbol{\Lambda}||_{\boldsymbol{V}_\Lambda} > 0, \ \ \forall\ \boldsymbol{\Lambda} \in \boldsymbol{V}_{\boldsymbol{\Lambda}}, \tag{3.10}$$

where $||\cdot||_{\boldsymbol{V}_U}$, $||\cdot||_{\boldsymbol{V}_P}$, and $||\cdot||_{\boldsymbol{V}_\Lambda}$ are the norms of the product spaces of the nodal displacement, pore pressure, and Lagrange multipliers, respectively. Notice that if β_s does not exist, then the kernel space of $\mathbb{B}$ may contain non-trivial basis. This non-trivial basis may cause spurious oscillations in the solution fields.

3.2. Discrete twofold inf–sup test

Having formulated the stability requirement as the twofold inf–sup condition (3.10), we now introduce a simple numerical procedure that can determine whether this condition is satisfied. The numerical procedure we propose here is an extension of the inf–sup test used in [73,74,81]. We emphasize that this numerical test by no means supersedes the analytical proof of the stability of nonlinear boundary value problems. However, because the analytical proof is notoriously difficult, here we aim at developing a practical means for investigating the existence of spurious modes at a given incremental step.

Let $\mathbb{I}^{\mathcal{S}}$ denote the matrix associated with the the scalar product of a finite element space $\mathcal{S}$ [38]. Following the standard procedure to establish an inf–sup test [33,74], we rewrite the twofold inf–sup condition (3.10) as

$$\begin{bmatrix}\boldsymbol{\Psi}_{\boldsymbol{u}} & \boldsymbol{\Psi}_p\end{bmatrix}\begin{bmatrix}\mathbb{C}_u & \mathbb{C}_p\end{bmatrix}\begin{bmatrix}\mathbb{I}^{\boldsymbol{V}_U} & \boldsymbol{0}\\ \boldsymbol{0} & \mathbb{I}^{\boldsymbol{V}_P}\end{bmatrix}\begin{bmatrix}\mathbb{C}_u^{\mathrm{T}}\\ \mathbb{C}_p^{\mathrm{T}}\end{bmatrix}\begin{bmatrix}\boldsymbol{\Psi}_{\boldsymbol{u}}\\ \boldsymbol{\Psi}_p\end{bmatrix} \geqslant \beta_s\begin{bmatrix}\boldsymbol{\Psi}_{\boldsymbol{u}} & \boldsymbol{\Psi}_p\end{bmatrix}\begin{bmatrix}\boldsymbol{\Psi}_{\boldsymbol{u}}\\ \boldsymbol{\Psi}_p\end{bmatrix}, \tag{3.11}$$

where $\boldsymbol{\Psi}_{\boldsymbol{u}} \in \mathbb{R}^{N_u} \setminus \{\boldsymbol{0}\}$ and $\boldsymbol{\Psi}_p \in \mathbb{R}^{N_p} \setminus \{\boldsymbol{0}\}$. The existence of the positive constant β_s is therefore guaranteed if the smallest eigenvalue of the following generalized eigenvalue problem is larger than zero:

$$\begin{bmatrix}\mathbb{C}_u & \mathbb{C}_p\end{bmatrix}\begin{bmatrix}\mathbb{I}^{\boldsymbol{V}_U} & \boldsymbol{0}\\ \boldsymbol{0} & \mathbb{I}^{\boldsymbol{V}_P}\end{bmatrix}\begin{bmatrix}\mathbb{C}_u^{\mathrm{T}}\\ \mathbb{C}_p^{\mathrm{T}}\end{bmatrix}\begin{bmatrix}\boldsymbol{\Psi}_{\boldsymbol{u}}\\ \boldsymbol{\Psi}_p\end{bmatrix} = \lambda_\beta\begin{bmatrix}\boldsymbol{\Psi}_{\boldsymbol{u}}\\ \boldsymbol{\Psi}_p\end{bmatrix}. \tag{3.12}$$

The square root of the minimum eigenvalue value of (3.12) is commonly referred to as the inf–sup value [33,73,74,81]. The inf–sup value is crucial and widely used in computational mechanics problems, as it enables one to easily detect the onset of spurious modes by checking whether the inf–sup value becomes zero. This procedure—checking the existence of a positive non-zero inf–sup value—is called the inf–sup test. This test involves the calculation of inf–sup values corresponding to the same boundary value problems discretized by typically at least four successively refined meshes. In the next section, we will conduct inf–sup tests for multiscale coupling operators $[\mathbb{C}_u\ \mathbb{C}_p]$ in various numerical examples to examine whether spurious oscillation mode(s) may occur in the overlapped domain(s).

DOI: 10.1002/nme

4. NUMERICAL EXAMPLES

This section presents numerical examples to verify the proposed multiscale hydro-mechanical model and demonstrate its performance. For verification of the model in terms of hydro-mechanical coupling, we first use the classical Terzaghi's consolidation problem of which an analytical solution exists. Subsequently, to verify the model under incompressible/compressible deformations in the undrained/drained conditions, we extend Cook's membrane problem to poroelasticity and compare the results with benchmark values of incompressible and compressible cases. Lastly, to demonstrate the performance of the Arlequin model whereby different models are coupled, we simulate fluid injection into a pre-existing crack of a porous medium coupling an isogeometric extend finite element model with a polynomial-based standard finite element model. In this example, the fluid–solid interactions in both the near-field and far-field of a pre-existing crack are concurrently simulated. To investigate the spatial stability of the model, in every example, we perform the inf–sup test described in the previous section.

4.1. Terzaghi's 1D consolidation problem

Terzaghi's 1D consolidation problem is one of the few poromechanics problems of which analytical solutions exist [82]. As such, this problem has been widely used as benchmark to verify poromechanical models in the literature [1,3,16,65]. In this study, we use this problem as the first benchmark problem to verify the proposed Arlequin formulation for coupled hydro-mechanical problems.

Figure 2 illustrates the domain configuration and boundary conditions of the boundary value problem. As for the boundary conditions for fluid flow, the top boundary is a zero pressure boundary where drainage is allowed. On the other hand, the bottom and lateral boundaries are impermeable, that is, no flux boundaries. The solid boundary conditions are imposed such that the material deforms in the vertical direction only: the top boundary is subjected to compressive stress of 90 kPa while the bottom boundary is fixed and the lateral boundaries are constrained horizontally. As a result, the problem is essentially one-dimensional, allowing for an analytical solution.

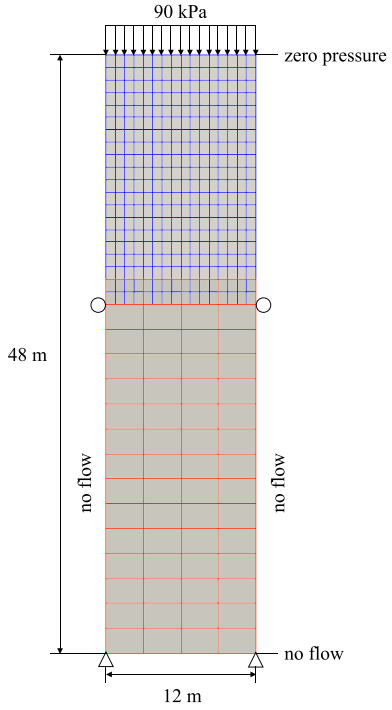

Figure 2. Domain configuration and boundary conditions of the 1D consolidation problem.

DOI: 10.1002/nme

We model the problem by overlapping two domains, as shown in Figure 2. Specifically, we discretize upper 45% of the domain by a finer mesh (fine domain) while discretize lower 65% by a coarser mesh (coarse domain). Both the coarse and fine domains are modeled by stabilized finite elements that use linear polynomials to interpolate the displacement and pore pressure fields and projection based strategy to stabilize the pore pressure field [45,51,52,75,77]. In the overlapped domain, each coarse-scale finite element is coupled with eight fine-scale finite elements. The H^1 coupling scheme is used throughout the verification simulations. The material parameters used in this problem are summarized in Table I.

The simulations are performed using two types of weighting functions: (1) constant weighting function and (2) linear weighting function. Figure 3 presents the results of the two cases in terms of the normalized pore pressure p/p_0 along the normalized location z/h where $p_0 = 90$ kPa. Here, we observe that the numerical solutions agree with the analytical solutions irrespective of the weighting functions.

Additional numerical experiments are conducted to investigate whether it is necessary to introduce constraints for both the displacement and pore pressure fields, not just for one of them. Figure 4(a) and 4(b) show the results when a constraint is applied to either the pore pressure or the displacement, respectively. As shown in Figure 4(a), the use of the pore pressure constraint alone is able to enforce the compatibility of pore pressures in the two domains, but it produces incorrect results. On the other hand, Figure 4(b) indicates that if the pore pressure constraint is not enforced, the coarse and fine pore pressure fields are not compatible with each other. These results demonstrate that both of the pore pressure and displacement constraints are essential to ensure the compatibility between the two domains.

Table I. Parameters for the 1D consolidation problem.

Parameter	Value	Unit
Young's modulus E	70	MPa
Poisson's ratio ν	0.4	–
Biot coefficient B	1.0	–
Porosity n	0.3	–
Permeability k	1.57×10^{-13}	m^2
Viscosity of pore fluid μ	1.0×10^{-3}	Pa · s
Bulk modulus of pore fluid K_f	2.2	GPa

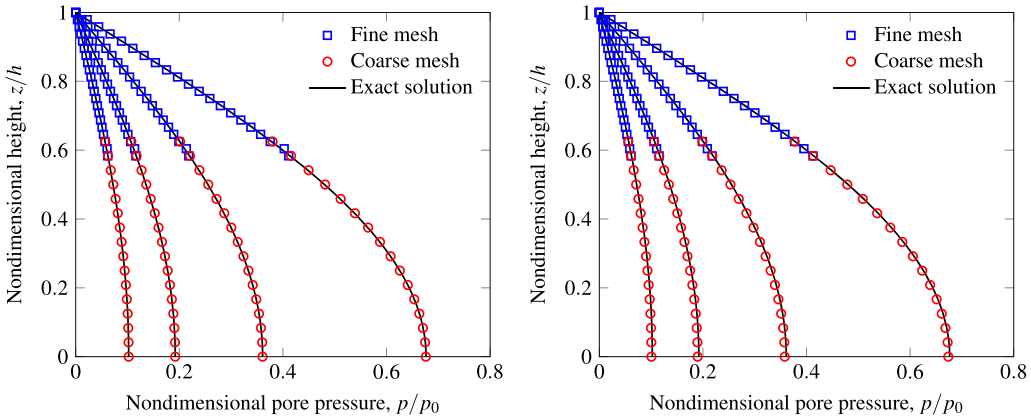

(a) Constant weighting function $\chi = 0.5$ **(b)** Linear weighting function

Figure 3. Pore pressure profiles of the 1D consolidation problem at 250, 500, 750, and 1000 s (from right to left in each figure), from the simulations employing: (a) constant weighting function and (b) linear weighting function.

DOI: 10.1002/nme

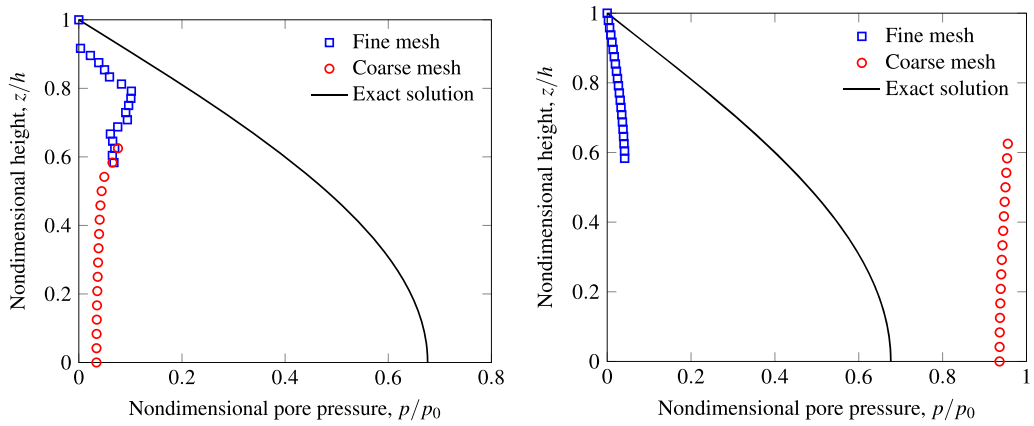

(a) Pressure constraint only **(b)** Displacement constraint only

Figure 4. Results of the consolidation problem (at time = 250 s) with different constraints: (a) Pressure constraint only and (b) Displacement constraint only.

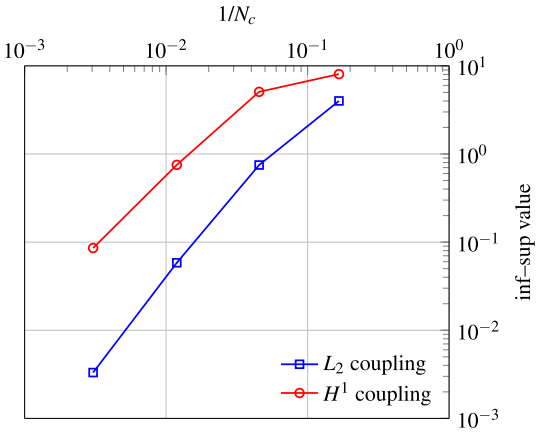

Figure 5. Inf–sup test results of the 1D consolidation problem.

4.1.1. Numerical inf–sup test for the 1D consolidation problem. To investigate the spatial stability of the proposed Arlequin method, we perform a numerical inf–sup test for this consolidation problem and present the results in Figure 5. We test both H^1 and L_2 coupling systems with a linear weighting function, and obtain the inf–sup values refining both the fine and coarse meshes. In this figure, N_c stands for the number of finite elements in the coarse domain. The results indicate that the H^1 coupling system always yields higher inf–sup values than the L_2 counterpart. Note that this observation is consistent with previous finding from a single-physics displacement-based Arlequin model [33]. The inf–sup values decrease with mesh refinement in both simulations. However, it is clear that the inf–sup value of the H^1 coupling performs better. As mentioned in [81], the inf–sup test is only considered successful when a lower bound of inf–sup values is likely to be found from underneath. However, in practice, the effectiveness of the inf–sup test, as explained and demonstrated through numerical examples in Bathe et al. [83], is highly sensitive to the norm one used to constructed in the inf–sup test. This is particularly true for problems that may exhibit boundary layer effect, such as Terzaghi's consolidation problem and convection–diffusion problems [84]. The difficulty of these problems is that at near time when the time step is small, the solution in the interior domain is smooth, while the solution near the boundary may exhibit sharp gradient. Hence, as mentioned in Bathe et al. [83], an ideal norm must be able to measure equally well in the smooth and non-smooth parts of the solution. This effective norm has not yet been found, according to the best knowledge of the authors, but we may consider it for future research. As a result, we may only

DOI: 10.1002/nme

draw the conclusion that the H^1 coupling strategy seems to generate more stable results than the L_2 counterpart, but it is not clear whether the inf−sup values will be bounded in either cases.

4.2. Modified Cook's membrane problem for poroelasticity

In the second example, we investigate the accuracy of the proposed Arlequin method when it is used to capture the transition from undrained to drained behaviors of a poroelastic medium. According to poroelasticity theory, a fluid-saturated porous solid may deform isochorically even if the solid matrix is compressible. This is possible if: (1) an incompressible fluid is trapped in the pore space because the loading rate is much higher than the hydraulic diffusivity, and (2) the solid and fluid constituents are both incompressible [51,85]. In other words, incompressibility can arise when the undrained bulk modulus approaches infinity despite the fact that the drained bulk modulus remains finite [86]. In the poromechanics and geotechnical engineering literature, this condition is usually referred to as the undrained condition, as opposed to the drained condition in which the pore fluid is free to migrate and the excess pore pressure is dissipated such that the presence of fluid in the pore space does not lead to an incompressibility constraint. These two distinctive types of isochoric or nearly isochoric deformation of porous media have been extensively studied and compared in Levenston et al. [87] and Sun et al. [51]. In the context of mixed finite elements for poromechanics, this incompressibility can trigger volumetric locking as well as spurious oscillations in the pore pressure field which was discussed in Section 3. However, how this incompressibility in the undrained condition can affect the convergence and stability of the proposed Arlequin coupling model is elusive, as the Arlequin framework has not yet been applied to a poromecahanics problem.

The specific purpose of this example is to investigate whether any convergence or stability problem arises during the transition from the undrained condition to the drained condition. For this purpose, we modify Cook's membrane problem [88], which has served as a benchmark problem in many studies to assess a numerical technique designed to prevent volumetric locking in solid mechanics problems. Figure 6 depicts the mesh and boundary conditions of the modified Cook's problem which is modeled by two overlapped domains as in the previous example. For our purpose, we model the membrane as a porous solid fully saturated by a (nearly) incompressible fluid. This allows the

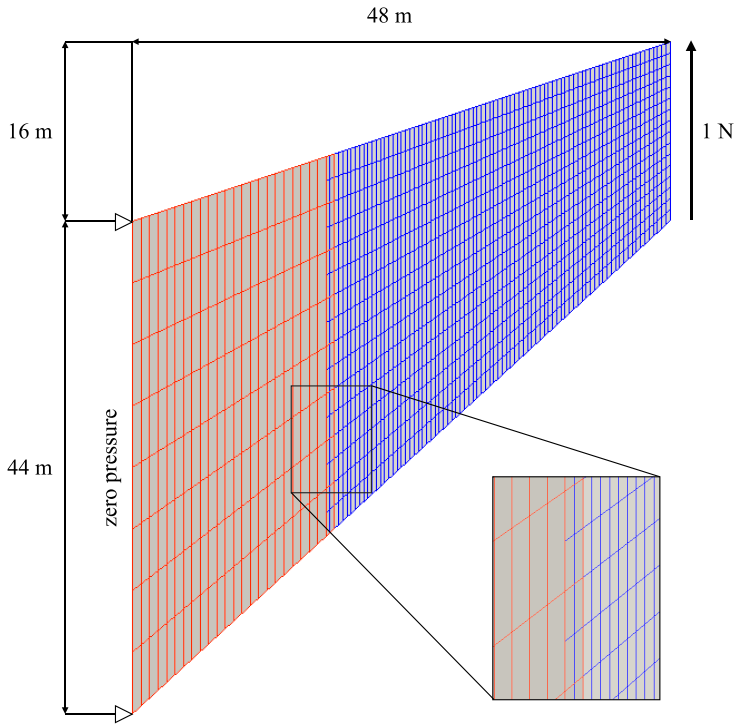

Figure 6. Domain configuration and boundary conditions of the modified Cook's membrane problem.

DOI: 10.1002/nme

membrane to be incompressible at the undrained limit without setting the Poisson ratio approaching 1/2. Meanwhile, the membrane may exhibit volumetric deformation as the excess pore pressure dissipates in time and eventually reaches the drained condition under which the membrane again behaves like a compressible material. The boundary conditions for the solid are identical to those of the original problem, and the traction applied to the right edge is 1 N. However, for the pore fluid, we introduce additional boundary conditions: the left edge is a zero pressure boundary while all other edges are no-flux boundaries.

The parameters for this problem are summarized in Table II. The material parameters for the solid are the same as those used in the classical Cook's membrane benchmark. On the other hand, the material parameters for the fluid (e.g., permeability) are chosen such that the material is subjected to the undrained condition after the first time step. We set the Poisson ratio of the solid matrix $\nu = 0.3$ so as to compare (1) the tip displacement in the undrained condition with the benchmark value in the incompressible case, and (2) the tip displacement in the drained condition with the benchmark value in the compressible case with $\nu = 0.3$.

Figure 7 presents the time evolution of the tip displacement after the loading. We observe that the displacement is about 16.5 m at the first time step and it converges to about 21.5 m with time. Note that the first time step is in the undrained condition while the final step is in the drained condition. The benchmark values of the tip displacement, which can be computed by Richardson's extrapolation [88], are found to be 16.43258437 m for the incompressible case ($\nu = 0.5$) and 21.5234479 m for the compressible case ($\nu = 0.3$). Figure 8 shows that the tip displacement converges to the benchmark values for both the incompressible (undrained) and compressible (drained) cases. In Figure 9, we also plot pore pressure fields in three time steps during the simulation. These contours indicate that the pore pressure developed by the tip loading is dissipated as time increases. The fact that both the deformation and pressure match well in the overlapped domain again demonstrates that the constraints used in the Arlequin model are appropriate.

Table II. Parameters for the modified Cook's membrane problem.

Parameter	Value	Unit
Young's modulus E	1	Pa
Poisson's ratio ν	0.3	–
Biot coefficient B	1.0	–
Porosity n	0.3	–
Permeability k	1.57×10^{-10}	m^2
Viscosity of pore fluid μ	1.0×10^{-3}	Pa · s
Bulk modulus of pore fluid K_f	2.2	GPa

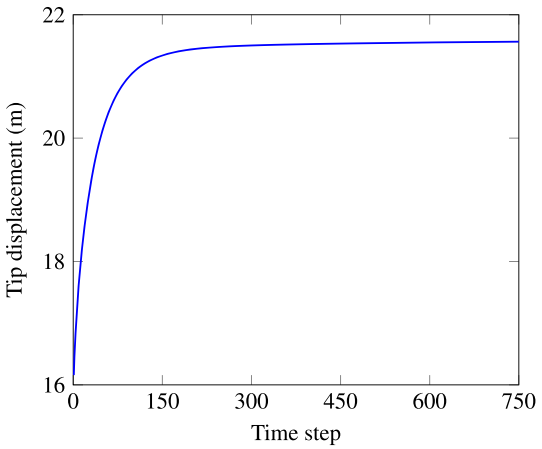

Figure 7. Tip displacement with time in the modified Cook's membrane problem.

DOI: 10.1002/nme

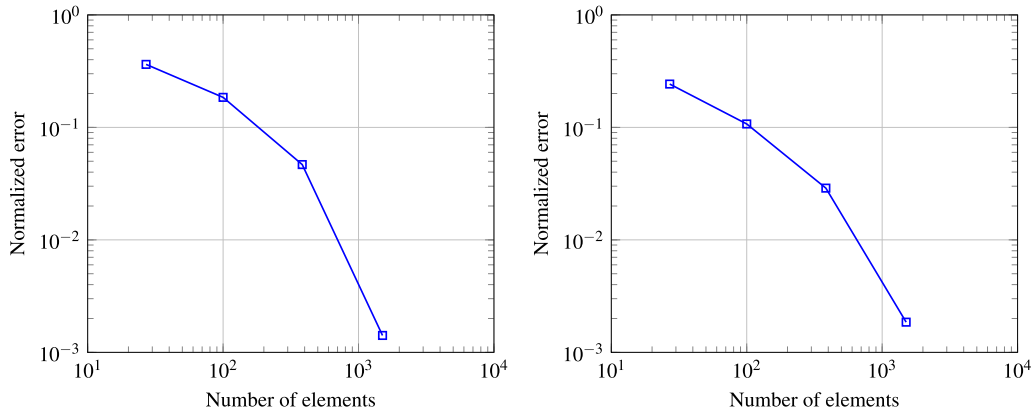

(a) Initial time step (incompressible/undrained) **(b)** Final time step (compressible/drained)

Figure 8. Normalized error of the tip displacement with mesh refinement: (a) Initial time step (incompressible/undrained) and (b) Final time step (compressible/drained).

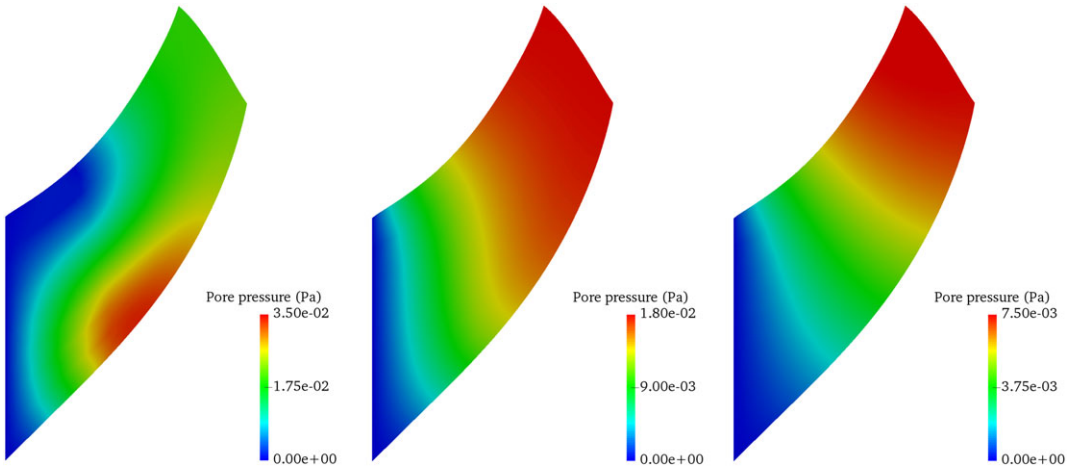

(a) Step #100 **(b)** Step #200 **(c)** Step #750

Figure 9. Pore pressure fields in the deformed membrane (magnification: 1x) at various time steps: (a) Step #100, (b) Step #200, and (c) Step #750.

4.2.1. Numerical inf–sup test for the modified Cook's membrane problem. We conduct two inf–sup tests for the modified Cook's membrane to investigate the effect of mesh ratio on the inf–sup values. In the first inf–sup test, we refine both the coarse and fine meshes three times and compute the inf–sup values for both the L_2 and H^1 coupling models. In all four simulations, the coarse-to-fine mesh ratio remains the same. Figure 10 shows the results of this constant mesh ratio inf–sup test. In this test, the inf–sup value decreases upon mesh refinement, similar to what we observed in the previous inf–sup test conducted for Terzaghi's problem.

In the second inf–sup test, we refine the fine mesh consecutively three times while keeping the coarse mesh size constant. As a result, upon the refinement, the coarse-to-fine mesh ratio decreases from 1:1 to 1:8. The inf–sup value of this changing-mesh-ratio inf–sup test is shown in Figure 11, where N_f represents the number of fine elements of the model. Surprisingly, the result suggests that the inf–sup value is not sensitive to the mesh ratio. This result suggests that the mesh ratio may have little influence on the spatial stability of the Arlequin poromechanics model. Further studies must be conducted to check whether this observation can be applied to other problems, but the relatively small changes in the inf–sup test indicate that coupling between models designed for significantly different length scales can be numerically stable.

DOI: 10.1002/nme

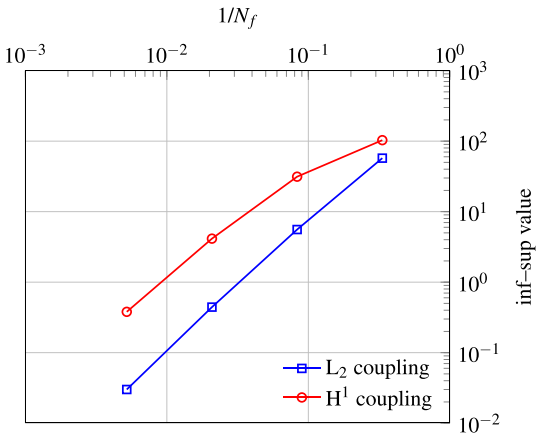

Figure 10. Inf–sup test results of the modified Cook's membrane problem with a constant mesh ratio.

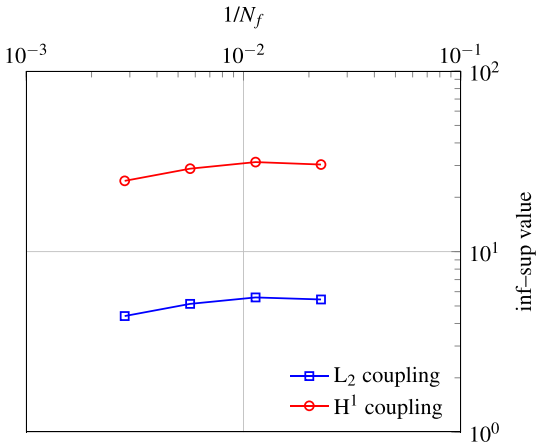

Figure 11. Inf–sup test results of the modified Cook's membrane problem with various coarse-to-fine mesh size ratios ranging from 1:1 to 1:8.

4.3. Fluid injection into a pre-existing crack of a porous medium

We consider the problem of fluid injection into a pre-existing crack of a porous medium, which arises in many applications including hydraulic fracturing, geological sequestration of fluidized greenhouse gases, and geological disposal of contaminants and hazardous wastes [89,90]. As pointed out recently by Kim and Selvadurai [90], previous work on the fluid injection problem often treats injection activities as a static process where the geological material is assumed to be elastic and the injection process is simulated by a distribution of dilatation acting inside the geological formation. A more rigorous treatment of this important problem is to simulate the fluid injection problem in the framework of poroelasticity, such that transient effect induced by the pore fluid diffusion inside the pre-existing crack and the porous medium and the undrained and drained behaviors at $t = 0$ and $t \to \infty$ are properly captured.

Unlike the previous examples in which the solutions in the coarse and fine domains are both interpolated by polynomial basis functions, in this example, we purposely assign different finite dimensional spaces to interpolate solution field in different regions. Having verified the Arlequin poromechanics model through two numerical examples that couple different meshes together, this setup provides us an opportunity to assess the robustness and stability of the Arlequin coupling techniques when the coupling domains are represented by different numerical methods.

In this problem, complicated processes are expected to be concentrated on a local region around the crack, whereas relatively simple processes may occur in regions far from the pre-existing crack.

DOI: 10.1002/nme

These treatments render the Arlequin method an efficient, attractive strategy for a fluid injection problem. For the same reasons, the Arlequin method is also an appealing choice for modeling other problems where one can easily identify a domain of interest (e.g., existing fault and flow barrier).

Figure 12 illustrates the configuration of the fluid injection problem. Here we inject a constant flux of 0.1 mm/s into a 4.5 m long horizontal crack, which is located at the center of the left edge of a poroelastic domain. While no flow is allowed through the rest of the left edge, drainage is allowed through all other boundaries where pore pressure is zero. As for the solid boundary conditions, the left edge is supported by horizontal rollers except the bottom node which is fixed for stability. Using symmetry, we model a half of the domain. Table III summarizes the material parameters.

We partition the domain into three sub-domains: one domain that accommodates the crack (fine domain) while the other domains that are continuous porous media (intermediate and coarse domains). As shown in Figure 12, the level of spatial discretization is highest in the cracked fine domain and gradually decreases with the distance from the crack. There are two overlapped

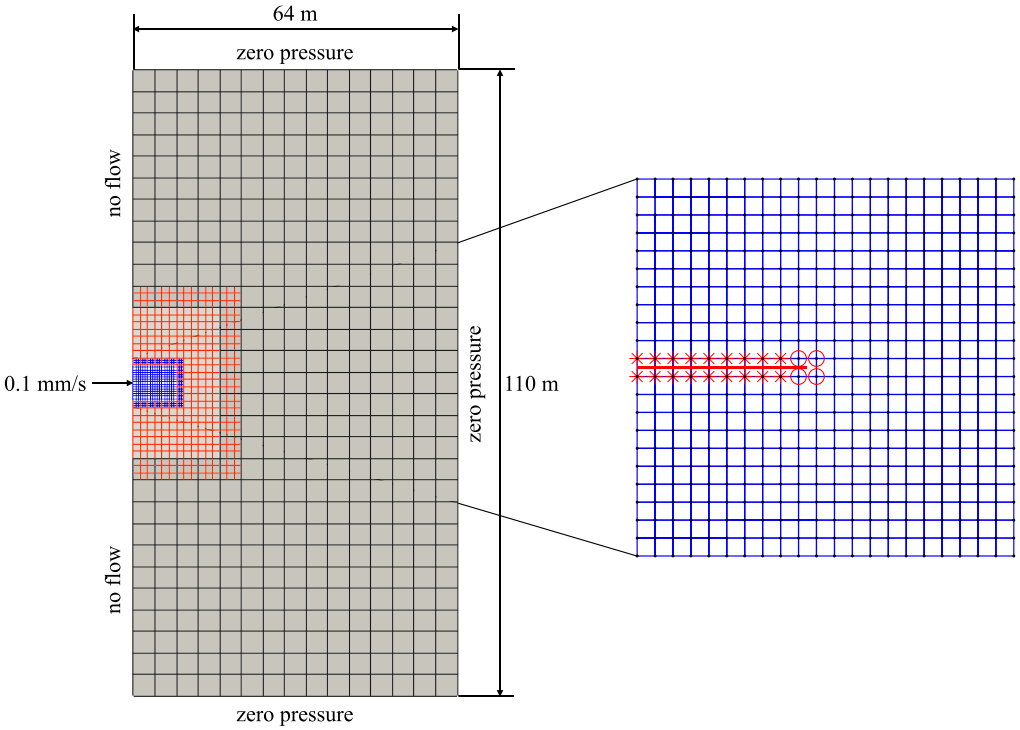

Figure 12. Domain configuration and boundary conditions for the fluid injection problem. The finest domain (zoomed mesh) is modeled by the isogeometric extended finite element method. Symbols in the zoomed mesh denote enriched nodes. Other domains are modeled by the polynomial-based standard finite element method. Because of the axial symmetry, only half of the domain is discretized and a zero horizontal displacement boundary condition is applied on the left side of the domain.

Table III. Parameters for the fluid injection problem.

Parameter	Value	Unit
Young's Modulus E	144	MPa
Poisson's ratio ν	0.2	-
Biot coefficient B	1.0	-
Porosity n	0.3	-
Permeability k	2×10^{-11}	m^2
Viscosity of pore fluid μ	1.0×10^{-3}	$Pa \cdot s$
Bulk modulus of pore fluid K_f	3.0	GPa

DOI: 10.1002/nme

domains—one linking the fine and the intermediate domains, and the other linking the intermediate and coarse domains. In these two overlapped domains, the finer meshes are conformal with the coarser meshes, and each coarser element is overlapped with nine finer elements in the gluing zone.

To take further advantage of the Arlequin method and to test the robustness of the Arlequin framework for coupling models of different natures, we employ different numerical methods and meshes of different sizes for the sub-domains in this last numerical example. For the cracked domain, we use the extended finite element method (XFEM) [91]—which allows one to capture strong discontinuity in the interior of finite elements without re-meshing—in conjunction with the isogeometric analysis (IGA) [92]—which interpolates solutions by non-uniform rational basis spline (NURBS) that can lead to higher-order accuracy than polynomial basis functions. It is worth noting that De Luycker et al. [93] and Verhoosel et al. [94] have pointed out IGA employing XFEM to represent strong discontinuities lead to higher asymptotic convergence rate and accuracy with the same amount of degree of freedoms, in comparison with XFEM with conventional finite elements of equal degree. Because of these appealing features, we combine XFEM and IGA to model the cracked fine domain. Meanwhile, we use only polynomial-based finite elements to model the far-field domain, as the sharp gradient is absent there. Therefore, we purposely use the standard, polynomial-based finite elements for these non-cracked sub-domains and test whether the coupling in the overlapped domain is stable during the simulation. Once again, we emphasize that the capability of applying different numerical methods in different regions—which in turn allows the modelers to confine highly sophisticated, yet cost-demanding models to the domains of interest—is a major advantage of the Arlequin method as previously pointed out in [27,28,33,38]. As demonstrated in this numerical example, this advantage is also extended to multi-physical problems if a proper coupling strategy is used.

Hydro-mechanical processes in the cavity are modeled following standard approaches in the literature (e.g., [95]). Using XFEM, we introduce additional global degrees of freedom to the elements that accommodate the crack (these enriched nodes are denoted by red symbols in Figure 12). The fluid flow along the crack is modeled by the cubic law, which assumes that the transmissivity of a flow channel is proportional to the cube of the hydraulic aperture in 3D and the square of the hydraulic aperture in plane strain 2D problem [96–99]. In this numerical example, we assume that the mechanical and hydraulic apertures are identical. Hence, the hydraulic aperture (denoted as h herein) is defined as the separation distance between the upper and lower surfaces of the crack. In a 2D plane strain setting, the intrinsic permeability of the fracture along the crack reads,

$$k_f = \frac{1}{f}\frac{h^2}{3\mu}, \tag{4.1}$$

where f is a coefficient, which is typically within the range of (1.04, 1.65), according to Mohammadnejad and Khoei [98]. In this numerical example, we set $f = 1$. For brevity, the details of the formulation and implementation are included in Appendix A. Our main focus here is to demonstrate the possibility of using the Arlequin method to couple domains modeled by the isogeometric XFEM and the classical polynomial-based finite element. As a result, the boundary value problem we intended to solve is simplified such that the pre-existing crack would not propagate and the deformation of the solid skeleton is infinitesimal. More complex problems close to the setup of a field-scale operation problem will be considered in the future. In addition, we acknowledge that the Arlequin coupling framework is sufficiently flexible to accommodate other numerical methods for modeling localized phenomena in porous media, such as the strong discontinuity approach that enhances local shape functions for strain and flow [10,12]. In other words, the use of XFEM in this example is just one of the many possible ways to capture localized displacement jump and fluid flow within the multi-model Arlequin framework.

Figures 13 and 14 show pore pressure and Darcy velocity fields at $t = 2$ and $t = 10$ s in deformed domains (deformations are magnified by 6000 times). The overall pressure and flow patterns indicate that the injection drives flow of the pore fluid into the drainage boundaries of the porous media. Because of the relatively high effective permeability of the the host matrix, the pore pressure field appears to be continuous and without sharp gradient. As the boundary layer of the pressure plume penetrates into the bulk materials, the pore pressure jump has not been observed even though the extended finite element formulation we adopted does include enhancement in the pore pressure field.

DOI: 10.1002/nme

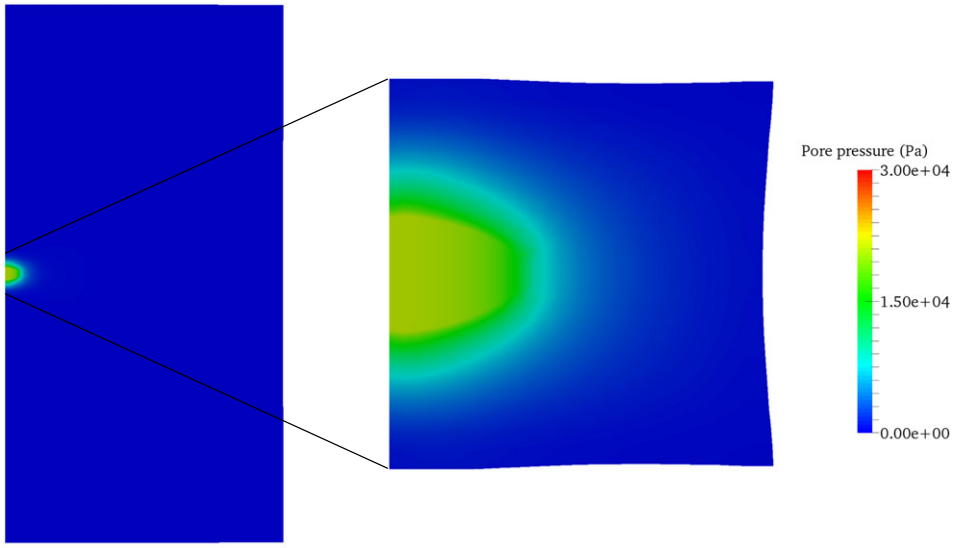

(a) At $t = 2$ s

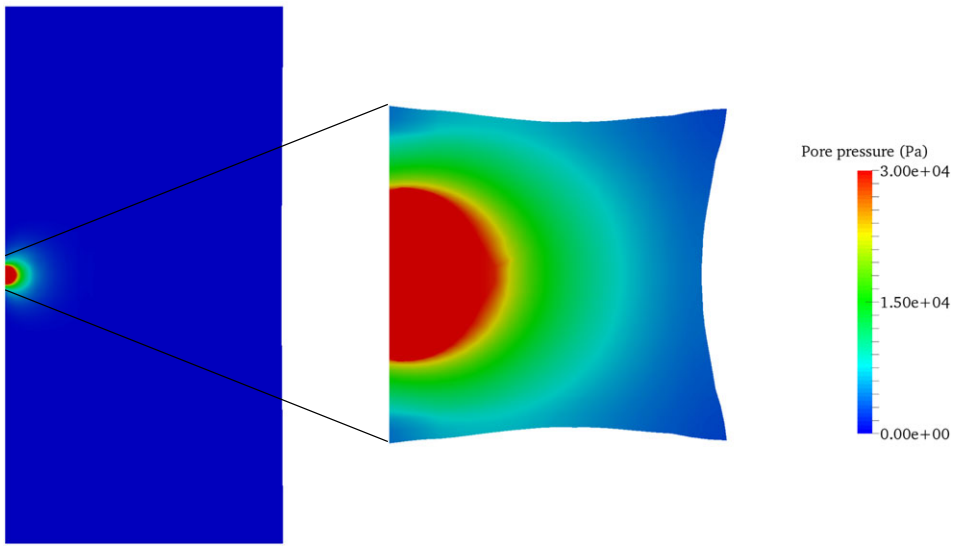

(b) At $t = 10$ s

Figure 13. Pore pressure field in the deformed domain (magnification: 6000x) modeled by the three-level mesh.

Further discussion on various modeling techniques for the fluid flow in embedded discontinuity can be found in [10,12,94], and in the recent review in de Borst [99], but it is out of the scope of this study which mainly focuses on Arlequin coupling models. We note that these injection-induced pressure build-up and flow are significant in near-fields of the crack but they are marginal in far-fields. In Figure 15, we show engineering shear strains at the same time instants. We observe that shear strains are developed in near-fields of the crack due to hydro-mechanical coupling between fluid injection and crack opening. Again, we see that shear strains are marginal in far-fields. These contrasting complexities of physical processes in the near and far-fields clearly justify the use of the Arlequin method for introducing different models to the near and far-fields.

To investigate the effects of hydro-mechanical interactions among near-fields and far-fields, we repeat the problem employing three levels of meshes, namely one-level, two-level, and three-level meshes. In the one-level mesh model, we simulate the fluid injection simulation only in the finest mesh. Then, we conduct the two-level mesh model by placing an additional (intermediate) mesh

DOI: 10.1002/nme

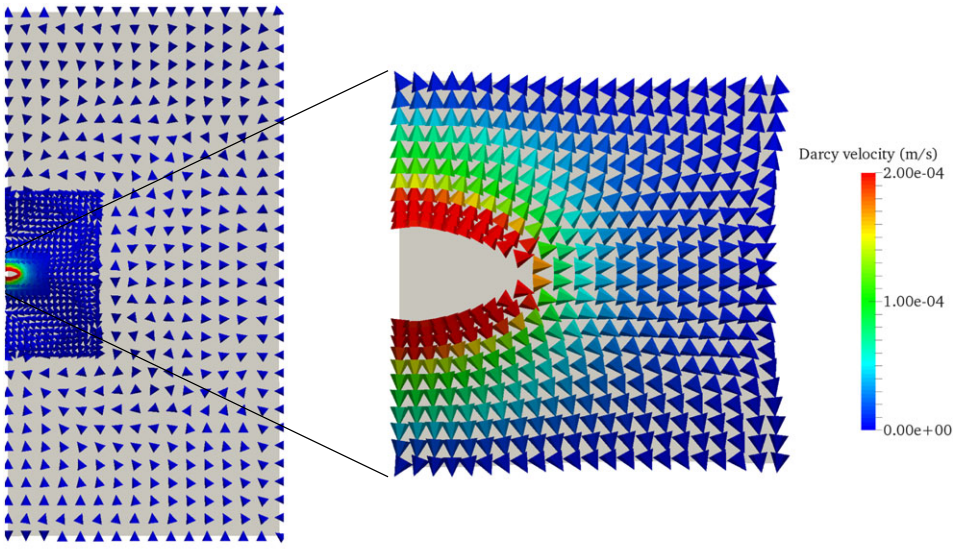

(a) At $t = 2$ s

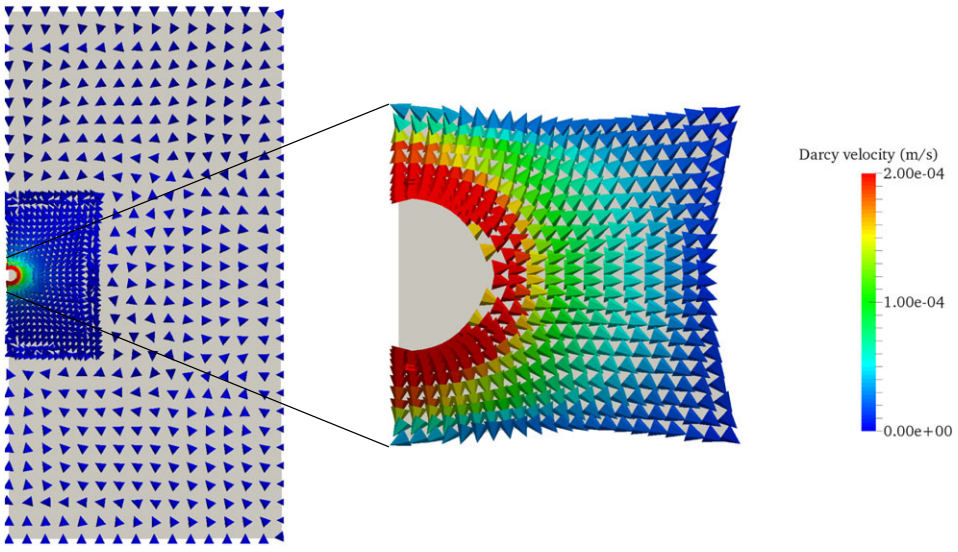

(b) At $t = 10$ s

Figure 14. Darcy velocity field in the deformed domain (magnification: 6000x) modeled by the three-level mesh.

and bundling it with the fine mesh to enlarge the domain. Finally, in the three-level mesh model, we continue to enlarge the domain by introducing the coarse mesh such that it coincides the model we have considered so far. In other words, all three models share the fine domain with the extended isogeometric finite element, and the two-level and three-level mesh models commonly employ the intermediate domain of the three-level mesh. Note that while the Arlequin method is not essential to place more degree of freedoms near the crack tip, it enables coupling different numerical methods (in this case NURBS-based XFEM and polynomial-based standard FEM), which is very challenging otherwise.

In Figure 16, we compare results of the three models in terms of opening displacements along the crack in the fine domain. Generally, models with larger domains tend to predict larger crack openings. This trend can be attributed to the fact that larger domains are less affected by boundary effects and thus closer to a poroelastic half space. At $t = 2$ s, the opening cracks of the two-level and three-level mesh models are almost identical; however, they become different as

DOI: 10.1002/nme

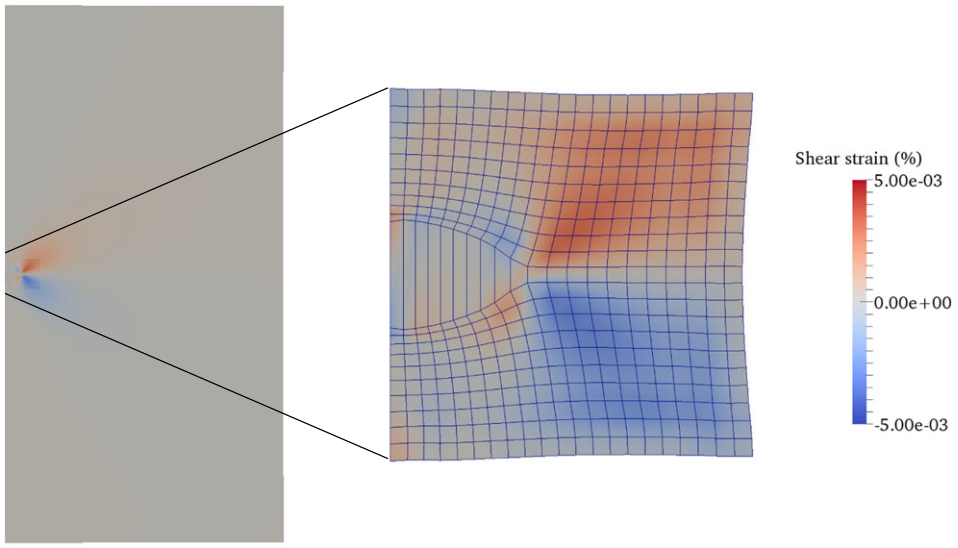

(a) At $t = 2$ s

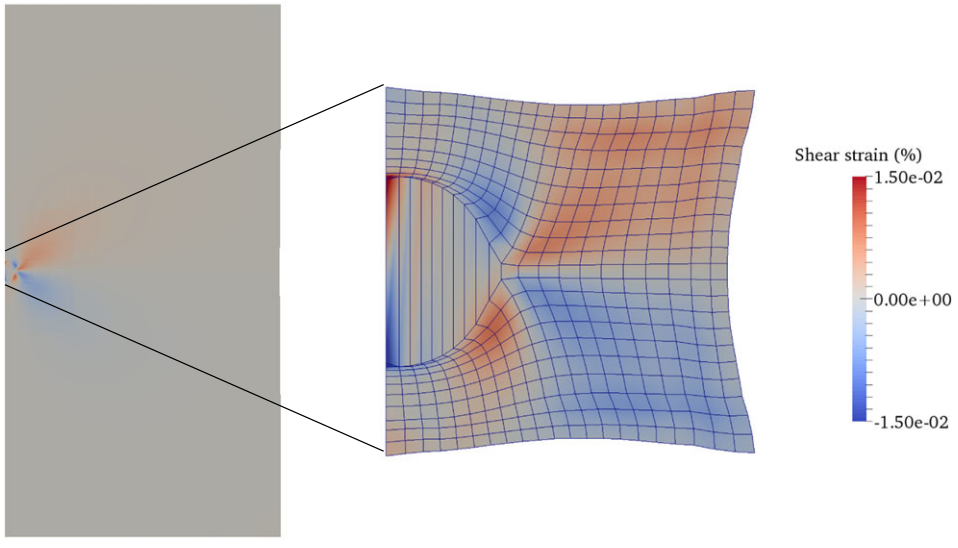

(b) At $t = 10$ s

Figure 15. Shear strain field in the deformed domain (magnification: 6000x) modeled by the three-level mesh.

time proceeds to $t = 10$ s. This observation indicates that the opening crack displacement grows faster in the model with the far-field than in the model with only the fine isogeometric domain.

Figure 17 shows the von Mises stress distribution behind the pre-existing crack (along the horizontal line that separate the upper and lower domains evenly). Because there is no traction-separation law employed at the interface, the von Mises stress is zero inside the crack. Unlike the pore pressure and displacement fields of which the existence of nodal values allows one to interpolate via the basis function, the stress tensor is only evaluated at the Gauss point. Hence, we use a L_2 projection scheme to project the discrete data point to the interpolated field spanned by the same basis functions we used to interpolate displacement and pore pressure [100,101]. For brevity, we will not provide details of the projection scheme. Interested readers are referred to Mota et al. [101] for details. As expected, the von Mises stress is concentrated near the crack tip and gradually decreases.

Figures 18 present the results of the three models in terms of the pore pressure along the crack. Note that as each coarse mesh is added, the numerical solution behaves closer to a poro-elastic half

DOI: 10.1002/nme

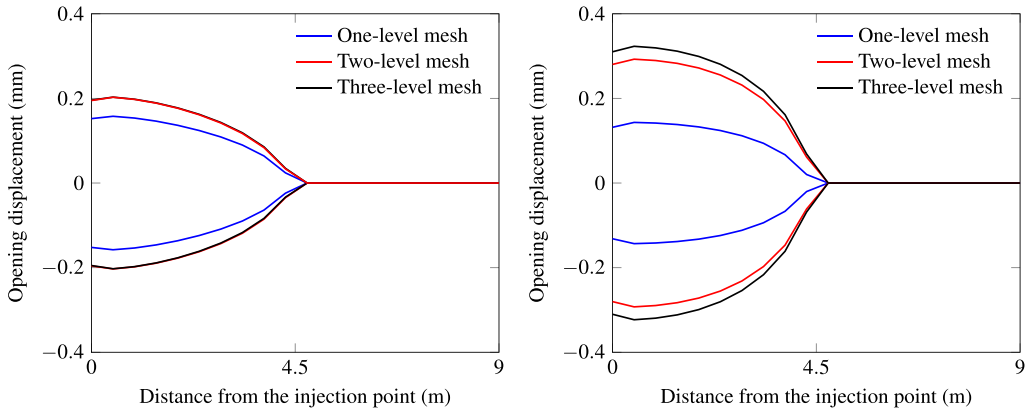

(a) At $t = 2$ s **(b)** At $t = 10$ s

Figure 16. Opening displacement along the crack: (a) $t = 2$ s and (b) $t = 10$ s.

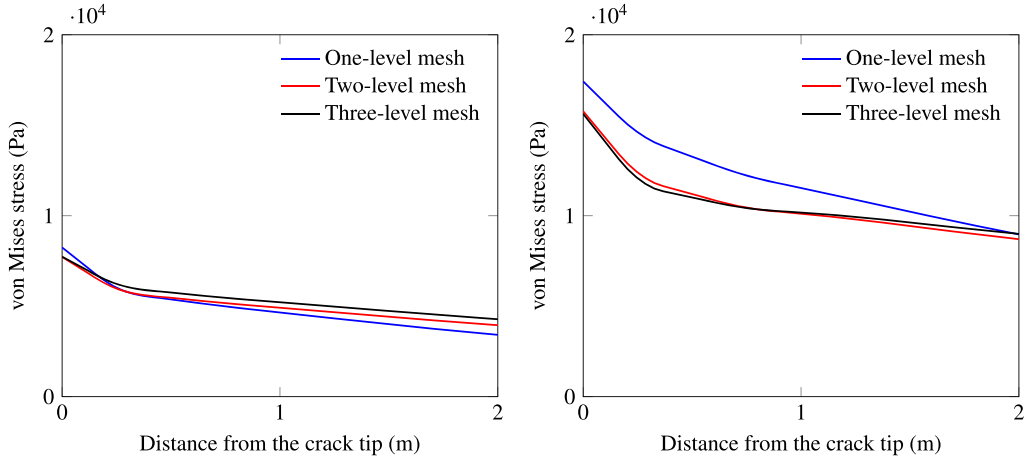

(a) At $t = 2$ s **(b)** At $t = 10$ s

Figure 17. Variation of von Mises stress behind the crack tip: (a) $t = 2$ s and (b) $t = 10$ s

space. While the pore pressure and the von Mises stress are different in all three cases, they show consistent trends with the increase of the level of meshes.

These findings from the three-level mesh study indicate that incorporating far-field effects can enhance the resolution of near field solutions. Yet in practical problems such incorporation of far-field can be prohibitively expensive without an efficient concurrent multiscale, multimodel approach like the Arlequin method. In this example, we just added 778 polynomial-based standard finite elements for incorporating far-field effects to the one-level mesh model. The added computational cost is a fraction of the pre-existing cost from the NURBS-based extended finite elements in the fine domain, let alone the cost of a naive extension that uses the same NURBS-based finite elements for far-fields. This minimized cost showcases the advantage of the Arlequin method for concurrent multiscale modeling.

4.3.1. Numerical inf–sup test for the fluid injection problem. For this fluid injection problem, we perform four inf–sup tests refining only the fine domain modeled by NURBS-based XFEM. During the test, the fine-to-coarse mesh ratio varies from 16:1 to 1:1. Figure 19 shows the results of the inf–sup tests for L_2 and H^1 coupling cases. We observe that H^1 coupling results in higher inf–sup values, consistent with previous findings [33,66]. More importantly, the absence of any significant drop in the inf–sup values confirms the stability of our Arlequin poromechanics model. This result

DOI: 10.1002/nme

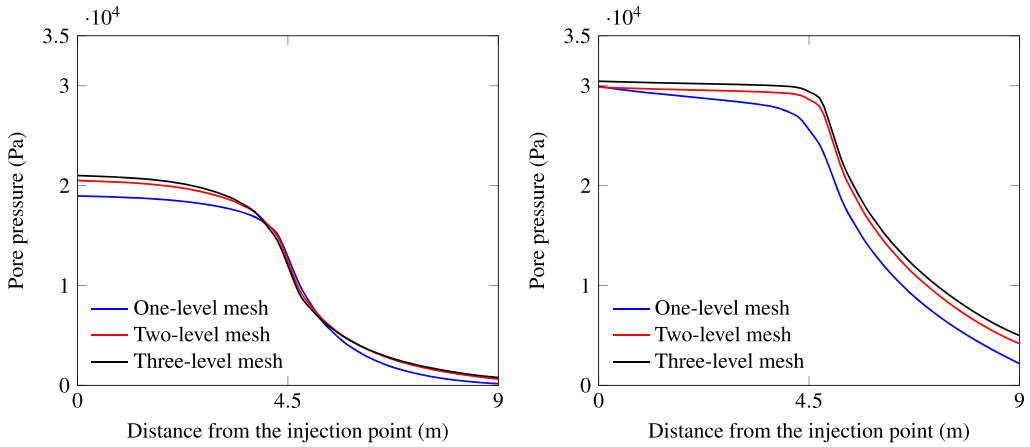

(a) At $t = 2$ s **(b)** At $t = 10$ s

Figure 18. Variation of pore pressure from the injection point: (a) $t = 2$ s and (b) $t = 10$ s.

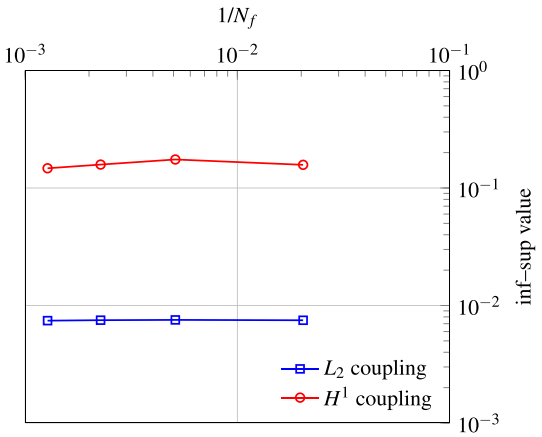

Figure 19. Inf–sup test results of the fluid injection problem.

is particularly encouraging, as it suggests that the numerical stability is insensitive to the mesh size ratio (in this case from 16:1 to 1:1) as well as the numerical methods (in this case from NURBS-based to polynomial-based finite elements) in the overlapped region. Generalizing this conclusion to other hydro-mechanical problems via a more rigorous mathematical analysis deserves future work.

5. CONCLUSION

A concurrent multiscale model for coupled poromechanics has been developed. Built on the Arlequin framework, this model enforces weak compatibility of displacement and pore pressure fields between domains by distributing energies. We have derived a necessary condition for spatial stability as a twofold inf–sup condition, and proposed a discrete twofold inf–sup test to check the numerical stability. Through two benchmark problems, we have verified the developed model under various refinement levels, mesh ratios, and drainage conditions. We have also presented a numerical example that couples NURBS-based and polynomial-based finite element models to simulate fluid injection into a cracked porous material. This example has demonstrated how the Arlequin model can couple different poromechanics models of multiple length scales in an efficient manner. This feature can significantly advance our modeling capabilities of emerging and complicated hydro-mechanical problems whereby highly contrasting processes take place at multiple scales and regions, such as those involving injection, shear banding, faulting, or fractures.

DOI: 10.1002/nme

APPENDIX A: FORMULATION OF THE ISOGEOMETRIC EXTENDED FINITE ELEMENTS IN THE FLUID INJECTION PROBLEM

This appendix describes the formulation of the isogeometric extended finite element model used in the fluid injection problem (Section 4.3). For more details, we refer to Nguyen et al. [102] and the open-source code base `igafem` with which we implement the Arlequin poromechanics model. In the following, we adopt the notation in Nguyen et al. [102]. First, let us construct a B-spline with a knot vector

$$\Xi = \{\xi_1, \xi_2, \ldots, \xi_{n+p+1}\}, \quad \xi_n \leqslant \xi_{n+1}, \tag{A1}$$

where ξ is the i-th knot, n is the number of B-spline basis function and p is the polynomial order. Then, the corresponding set of B-spline basis functions can be defined by the Cox-de-Boor formula, for the zeroth order basis function ($p = 0$):

$$N_{i,0}(\xi) = \begin{cases} 1 & , \text{ if } \xi_i \leqslant \xi \leqslant \xi_{i+1}, \\ 0 & , \text{ otherwise,} \end{cases} \tag{A2}$$

and for a polynomial order $p \geqslant 1$

$$N_{i,p}(\xi) = \frac{\xi - \xi_i}{\xi_{i+p} - \xi_i} N_{i,p-1}(\xi) + \frac{\xi_{i+p+1} - \xi}{\xi_{i+p+1} - \xi_{i+1}} N_{i+1,p-1}(\xi), \tag{A3}$$

where the fractions with the form $0/0$ are defined as zero. Therefore, the NURBS basis function can be defined as follows:

$$R_{i,p}(\xi) = \frac{N_{i,p}(\xi)\omega_i}{W(\xi)} = \frac{N_{i,p}(\xi)\omega_i}{\sum_{\hat{\imath}=1}^{n} \omega_{\hat{\imath}}}, \tag{A4}$$

where $\omega_i > 0$ is the set of NURBS weights.

Employing these NURBS shape functions and the extended finite element method, we express the two-dimensional displacement field in the cracked elements as follows:

$$\boldsymbol{u}^h(\boldsymbol{x}) = \sum_{I \in \mathcal{S}} R_I(\boldsymbol{x}) \boldsymbol{u}_I + \sum_{J \in \mathcal{S}^c} R_J(\boldsymbol{x}) H(\boldsymbol{x}) \boldsymbol{a}_J + \sum_{K \in \mathcal{S}^f} R_K(\boldsymbol{x}) \left(\sum_{\alpha=1}^{4} B_\alpha \boldsymbol{b}_K^\alpha \right), \tag{A5}$$

where $R_{I,J,K}$ are the NURBS basis functions defined previously, $\boldsymbol{u}_I$ represents the standard degrees of freedom for the displacement, $\boldsymbol{a}_J$ the enrichment degrees of freedom for the crack, and $\boldsymbol{b}_K^\alpha$ the enrichment degrees of freedom for the crack tip. The set $\mathcal{S}$ includes the standard points, while the set $\mathcal{S}^c$ includes the control points/nodes whose supports are cut by the crack and the set $\mathcal{S}^f$ are control points with the crack tip. $H(\boldsymbol{x})$ is the Heaviside function given by:

$$H(\boldsymbol{x}) = \begin{cases} +1 & , \text{ if } (\boldsymbol{x} - \boldsymbol{x}^*) \cdot \boldsymbol{n} \geqslant 0, \\ -1 & , \text{ otherwise,} \end{cases} \tag{A6}$$

where $\boldsymbol{n}$ is the outward normal vector to the crack and $\boldsymbol{x}^*$ denotes the projection of point $\boldsymbol{x}$ on the crack. The branch functions B_α, which span the crack tip displacement field, are defined as follows:

$$[B_1, B_2, B_3, B_4](r, \theta) = \left[\sqrt{r}\, \sin\frac{\theta}{2},\ \sqrt{r}\, \cos\frac{\theta}{2},\ \sqrt{r}\, \sin\frac{\theta}{2}\, \cos\theta,\ \sqrt{r} \cos\frac{\theta}{2}\, \cos\theta \right], \tag{A7}$$

Here r and θ are the polar coordinates in the local crack front. Accordingly, now the strain–displacement matrix $\boldsymbol{B}$ accommodates the enrichment degrees of freedom as follows:

$$\boldsymbol{B} = [\boldsymbol{B}^{\text{std}} \mid \boldsymbol{B}^{\text{enr}}], \tag{A8}$$

where $\boldsymbol{B}^{\text{std}}$ is the $\boldsymbol{B}$ matrix related to the standard degrees of freedom while $\boldsymbol{B}^{\text{enr}}$ is that related to the enrichment degree of freedoms. This enriched strain–displacement matrix is thus a function

DOI: 10.1002/nme

of both the NURBS basis functions and the global enrichment introduced to represent the strong discontinuity (crack). In two-dimensional case, this enriched strain–displacement matrix is given by

$$\boldsymbol{B}_I^{\text{enr}} = \begin{bmatrix} (R_I)_{,x}\Psi_I + R_I(\Psi_I)_{,x} & 0 \\ 0 & (R_I)_{,y}\Psi_I + R_I(\Psi_I)_{,y} \\ (R_I)_{,y}\Psi_I + R_I(\Psi_I)_{,y} & (R_I)_{,x}\Psi_I + R_I(\Psi_I)_{,x} \end{bmatrix}. \tag{A9}$$

Depending on whether control point I near the tip is enriched, Ψ_I can be either the branch functions B_α or the Heaviside function H. In Armero and Callari [10] and Réthoré et al. [96], the pore pressure is assumed to remain continuous, while a jump may exist in the Darcy's velocity component normal to the crack faces. As recently explained in de Borst [99], this assumption can be relaxed such that the pore pressure itself can be discontinuous within the content of extended finite elements [99,103]. This approach is adopted in this study. To accommodate the strong discontinuity in the pore pressure field, we also introduce global enrichment to the pore pressure solution field. In the element where the strong discontinuity exists, the discrete gradient operator $\boldsymbol{B}^p$ is replaced by an enriched discrete gradient operator given by

$$\boldsymbol{B}^P = [\boldsymbol{B}^{\text{std},P} \mid \boldsymbol{B}^{\text{enr,P}}], \tag{A10}$$

where $\boldsymbol{B}^{\text{std},P}$ is the standard gradient matrix $\boldsymbol{B}^P$ while $\boldsymbol{B}^{\text{enr},P}$ is the enriched $\boldsymbol{B}^P$ matrix for the enriched pore pressure degree of freedom, that is,

$$\boldsymbol{B}_I^{\text{enr},P} = \begin{bmatrix} (R_I)_{,x}\Psi_I + R_I(\Psi_I)_{,x} \\ (R_I)_{,y}\Psi_I + R_I(\Psi_I)_{,y} \end{bmatrix}. \tag{A11}$$

The permeability inside the crack is modeled by the cubic law which relates the intrinsic permeability along the crack to cubic of the crack aperture. In this work, we employ an implicit scheme and defines the residual vector $\boldsymbol{R}_i$ at the i-th iteration as follows:

$$\boldsymbol{R}_i^{n+1} = \begin{bmatrix} \boldsymbol{0} & \boldsymbol{0} & \mathbb{C}_u^{\mathrm{T}} \\ \mathbb{G} & \mathbb{D}^{(1)} & \mathbb{C}_p^{\mathrm{T}} \\ \mathbb{C}_u & \mathbb{C}_p & \boldsymbol{0} \end{bmatrix} \begin{bmatrix} \Delta\hat{\boldsymbol{U}}_i^{n+1} \\ \Delta\hat{\boldsymbol{P}}_i^{n+1} \\ \Delta\boldsymbol{\Lambda}_i^{n+1} \end{bmatrix}_i + \begin{bmatrix} \mathbb{K} & \mathbb{G}^{\mathrm{T}} & \mathbb{C}_u^{\mathrm{T}} \\ \boldsymbol{0} & \Delta t\mathbb{D}^{(2)} & \mathbb{C}_p^{\mathrm{T}} \\ \mathbb{C}_u & \mathbb{C}_p & \boldsymbol{0} \end{bmatrix} \begin{bmatrix} \hat{\boldsymbol{U}}_i^{n+1} \\ \hat{\boldsymbol{P}}_i^{n+1} \\ \boldsymbol{\Lambda}_i^{n+1} \end{bmatrix}_i + \begin{bmatrix} \boldsymbol{F}_{\text{inter}}^n \\ \Delta t\boldsymbol{Q}_{\text{inter}}^n \\ \boldsymbol{0} \end{bmatrix}_i - \begin{bmatrix} \boldsymbol{F}_{\text{ext}}^n \\ \Delta t\boldsymbol{Q}_{\text{ext}}^n \\ \boldsymbol{0} \end{bmatrix}_i, \tag{A12}$$

where the subscript i in (A12) denotes the iteration, and $\mathbb{D}^1$ and $\mathbb{D}^2$ refer to the terms related to the local change of pore pressure and the diffusion-induced change of pore pressure, respectively. Here, the traction across the interior discontinuity is given by

$$\begin{aligned} \boldsymbol{F}_{\text{inter}} = & \int_{\Gamma_d} \chi[|\overline{\boldsymbol{N}}|]^{\mathrm{T}}\overline{\boldsymbol{t}_d}d\Gamma - \chi\left(\int_{\Gamma_d}[|\overline{\boldsymbol{N}}|]^{\mathrm{T}}\boldsymbol{n}_{\Gamma d}\overline{\boldsymbol{N}}d\Gamma\right)\overline{\boldsymbol{P}} \\ & + \int_{\Gamma_d}(1-\chi)[|\tilde{\boldsymbol{N}}|]^{\mathrm{T}}\widetilde{\boldsymbol{t}_d}d\Gamma - (1-\chi)\left(\int_{\Gamma_d}[|\tilde{\boldsymbol{N}}|]^{\mathrm{T}}\boldsymbol{n}_{\Gamma d}\tilde{\boldsymbol{N}}d\Gamma\right)\tilde{\boldsymbol{P}}, \end{aligned} \tag{A13}$$

along Γ_d where enriched nodes exist. Similarly, the interfacial flux vector is given by

$$\boldsymbol{Q}_{\text{inter}} = \int_{\Gamma_d}\chi\overline{\boldsymbol{N}}^{\mathrm{T}}\boldsymbol{n}_{\Gamma d}\overline{\boldsymbol{q}_d}d\Gamma + \int_{\Gamma_d}(1-\chi)\tilde{\boldsymbol{N}}^{\mathrm{T}}\boldsymbol{n}_{\Gamma d}\widetilde{\boldsymbol{q}_d}d\Gamma, \tag{A14}$$

where $\boldsymbol{n}_{\Gamma_d}$ denotes the unit normal vector of the interface Γ_d, $\overline{t_d}$ and $\widetilde{t_d}$ denote the cohesive tractions across the interface between the coarse and fine sub-domains, which vanish for a open crack, $\overline{\boldsymbol{q}_d}$ and $\widetilde{\boldsymbol{q}_d}$ are the fluid fluxes along the interface in the coarse and fine sub-domains.

DOI: 10.1002/nme

ACKNOWLEDGMENTS

The authors thank graduate student SeonHong Na for reviewing this manuscript. This research is financially supported by the Earth Materials and Processes program at the US Army Research Office under grant contract W911NF-14-1-0658 and W911NF-15-1-0581, the National Science Foundation under grant contracts CMMI-1462760 and EAR-1516300, and Sandia National Laboratories under grant contact PO-1557089. These supports are gratefully acknowledged. Sandia National Laboratories is a multi-mission laboratory managed and operated by Sandia Corporation, a wholly owned subsidiary of Lockheed Martin Corporation, for the US Department of Energy's National Nuclear Security Administration under contract DE-AC04-94AL85000. The authors are also grateful to the two anonymous reviewers for their detailed reviews and insightful suggestions.

REFERENCES

1. Zienkiewicz OC, Chan A, Pastor M, Schrefler B, Shiomi T. *Computational geomechanics with special reference to earthquake engineering*. Wiley: West Sussex, England, 1999.
2. Cowin SC. Bone poroelasticity. *Journal of Biomechanics* 1999; **32**(3):217–238.
3. Coussy O. *Poromechanics*. Wiley: West Sussex, England, 2004.
4. Sun W, Andrade JE, Rudnicki JW, Eichhubl P. Connecting microstructural attributes and permeability from 3D tomographic images of in situ shear-enhanced compaction bands using multiscale computations. *Geophysical Research Letters* 2011; **38**(10):L10302.
5. Sun W, Andrade JE, Rudnicki JW. Multiscale method for characterization of porous microstructures and their impact on macroscopic effective permeability. *International Journal for Numerical Methods in Engineering* 2011; **88**(12):1260–1279.
6. Wang K, Sun W. Anisotropy of a tensorial Bishop's coefficient for wetted granular materials. *Journal of Engineering Mechanics* 2015:B4015004.
7. Aubertin P, Réthoré J, de Borst R. Energy conservation of atomistic/continuum coupling. *International Journal for Numerical Methods in Engineering* 2009; **78**(11):1365–1386.
8. Fleck N, Hutchinson J. A reformulation of strain gradient plasticity. *Journal of the Mechanics and Physics of Solids* 2001; **49**(10):2245–2271.
9. Borja RI. A finite element model for strain localization analysis of strongly discontinuous fields based on standard galerkin approximation. *Computer Methods in Applied Mechanics and Engineering* 2000; **190**(11–12):1529–1549.
10. Armero F, Callari C. An analysis of strong discontinuities in a saturated poro-plastic solid. *International Journal for Numerical Methods in Engineering* 1999; **46**(10):1673–1698.
11. Borja RI. Finite element simulation of strain localization with large deformation: capturing strong discontinuity using a petrov-galerkin multiscale formulation. *Computer Methods in Applied Mechanics and Engineering* 2002; **191**(27–28):2949–2978.
12. Callari C, Armero F, Abati A. Strong discontinuities in partially saturated poroplastic solids. *Computer Methods in Applied Mechanics and Engineering* 2010; **199**(23):1513–1535.
13. Feyel F. A multilevel finite element method (FE^2) to describe the response of highly non-linear structures using generalized continua. *Computer Methods in Applied Mechanics and Engineering* 2003; **192**(28–30):3233–3244.
14. Belytschko T, Loehnert S, Song J-H. Multiscale aggregating discontinuities: a method for circumventing loss of material stability. *International Journal for Numerical Methods in Engineering* 2008; **73**(6):869–894.
15. Liu Y, Sun W, Yuan Z, Fish J. A nonlocal multiscale discrete-continuum model for predicting mechanical behavior of granular materials. *International Journal for Numerical Methods in Engineering* 2016; **106**(2):126–160.
16. Wang K, Sun W. A semi-implicit discrete-continuum coupling method for porous media based on the effective stress principle at finite strain. *Computer Methods in Applied Mechanics and Engineering* 2016; **304**:546–583.
17. Wang K, Sun W. A Semi-Implicit Micropolar Discrete-to-Continuum Method for Granular Materials. In *Proceedings of European Congress on Computational Methods in Applied Science and Engineering*, Papadrakakis M, Papadopoulos V, Stefanou G, Plevris V (eds). National Technical University of Athens (NTUA): Crete Island, Greece; June 5–10, 2016.
18. Wang K, Sun W, Salager S, Na S, Khaddour G. Identifying material parameters for a micro-polar plasticity model via X-ray micro-CT images: lessons learned from the curve-fitting exercises. *International Journal for Multiscale Computational Engineering* 2016; **14**(4):389–413.
19. Kouznetsova V, Geers M, Brekelmans W. Multi-scale second-order computational homogenization of multi-phase materials: a nested finite element solution strategy. *Computer Methods in Applied Mechanics and Engineering* 2004; **193**(48–51):5525–5550.
20. Ehlers W, Ramm E, Diebels S, d'Addetta G. From particle ensembles to cosserat continua: homogenization of contact forces towards stresses and couple stresses. *International Journal of Solids and Structures* 2003; **40**(24):6681–6702.
21. White J, Borja R, Fredrich J. Calculating the effective permeability of sandstone with multiscale lattice Boltzmann/finite element simulations. *Acta Geotechnica* 2006; **1**:195–209.
22. Lenoir N, Andrade J, Sun W, Rudnicki J. In situ permeability measurements inside compaction bands using X-ray CT and lattice Boltzmann calculations. *Advances in Computed Tomography for Geomaterials: GeoX2010* 2010:279–286.

DOI: 10.1002/nme

23. Sun W, Kuhn MR, Rudnicki JW. A multiscale DEM–LBM analysis on permeability evolutions inside a dilatant shear band. *Acta Geotechnica* 2013:1–16.
24. Belgacem FB. The Mortar finite element method with Lagrange multipliers. *Numerische Mathematik* 1999; **84**:173–197.
25. Girault G, Galmiche JM. Further study of nucleotide-binding site on chloroplast coupling factor 1. *European Journal of Biochemistry* 1977; **77**:501–510.
26. Ben Dhia H. Multiscale mechanical problems: the Arlequin method. *Comptes Rendus de l'Academie des Sciences Series IIB Mechanics Physics Astronomy* 1998; **326**(12):899–904.
27. Ben Dhia H, Rateau G. The Arlequin method as a flexible engineering design tool. *International Journal for Numerical Methods in Engineering* 2005; **62**(11):1442–1462.
28. Bauman P, Ben Dhia H, Elkhodja N, Oden J, Prudhomme S. On the application of the Arlequin method to the coupling of particle and continuum models. *Computational Mechanics* 2008; **42**:511–530.
29. Dhia HB. Further insights by theoretical investigations of the multiscale Arlequin method. *International Journal for Multiscale Computational Engineering* 2008; **6**(3):215–232.
30. Jamond O, Ben H. On the use of XFEM within the Arlequin framework for the simulation of crack propagation. *Computer Methods in Applied Mechanics and Engineering* 2010; **199**:1403–1414.
31. Bauman P, Oden J, Prudhomme S. Adaptive multiscale modeling of polymeric materials with Arlequin coupling and goals algorithms. *Computer Methods in Applied Mechanics and Engineering* 2009; **198**(5):799–818.
32. Han F, Lubineau G. Coupling of nonlocal and local continuum models by the Arlequin approach. *International Journal for Numerical Methods in Engineering* 2012; **89**(6):671–685.
33. Sun W, Mota A. A multiscale overlapped coupling formulation for large-deformation strain localization. *Computational Mechanics* 2014; **54**(3):803–820.
34. DiMaio SP, Salcudean SE. Needle insertion modeling and simulation. *IEEE Transactions on Robotics and Automation* 2003; **19**(5):864–875.
35. Detournay E. Mechanics of hydraulic fractures. *Annual Review of Fluid Mechanics* 2016; **48**:311–339.
36. Juanes R, Jha B, Hager BH, Shaw JH, Plesch A, Astiz L, Dieterich JH, Frohlich C. Were the May 2012 Emilia-Romagna earthquakes induced? A coupled flow-geomechanics modeling assessment. *Geophysical Research Letters* 2016; **43**(13):6891–6897.
37. Prudhomme S, Ben Dhia H, Bauman P, Elkhodja N, Oden J. Computational analysis of modeling error for the coupling of particle and continuum models by the Arlequin method. *Computer Methods in Applied Mechanics and Engineering* 2008; **197**(41–42):3399–3409.
38. Jamond O, Ben Dhia H. Incompressibility in the multimodel Arlequin framework. *International Journal for Numerical Methods in Engineering* 2013; **94**:374–399.
39. Wang H. *Theory of Linear Poroelasticity with Applications to Geomechanics and Hydrogeology*. Princeton University Press: Princeton, New Jersey, 2000.
40. Callari C, Abiati A. Hyperelastic multiphase porous media with strain-dependent retention laws. *Transport in Porous Media* 2011; **86**(1):155–176.
41. Geertsma J. A remark on the analogy between thermoelasticity and the elasticity of saturated porous media. *Journal of the Mechanics and Physics of Solids* 1957; **6**(1):13–16.
42. Nur A, Byerlee J. An exact effective stress law for elastic deformation of rock with fluids. *Journal of Geophysical Research* 1971; **76**(26):6414–6419.
43. Detournay E, Cheng A. Fundamentals of Poroelasticity. *Pergamon* 1993; **2**:chap. 5. 113–171.
44. Andrade JE, Borja RI. Modeling deformation banding in dense and loose fluid-saturated sands. *Finite Elements in Analysis and Design* 2007; **43**(5):361–383.
45. Sun W, Chen Q, Ostien J. Modeling the hydro-mechanical responses of strip and circular punch loadings on water-saturated collapsible geomaterials. *Acta Geotechnica* 2014; **9**(5):903–934.
46. Prévost JH. Nonlinear transient phenomena in saturated porous media. *Computer Methods in Applied Mechanics and Engineering* 1982; **30**(1):3–18.
47. Miehe C, Mauthe S, Teichtmeister S. Minimization principles for the coupled problem of Darcy–Biot-type fluid transport in porous media linked to phase field modeling of fracture. *Journal of the Mechanics and Physics of Solids* 2015; **86**:186–217.
48. Jha B, Juanes R. A locally conservative finite element framework for the simulation of coupled flow and reservoir geomechanics. *Acta Geotechnica* 2007; **2**(3):139–153.
49. Jeremić B, Cheng Z, Taiebat M, Dafalias Y. Numerical simulation of fully saturated porous materials. *International Journal for Numerical and Analytical Methods in Geomechanics* 2008; **32**(13):1635–1660.
50. Borja RI, Alarcón E. A mathematical framework for finite strain elastoplastic consolidation Part 1: Balance laws, variational formulation, and linearization. *Computer Methods in Applied Mechanics and Engineering* 1995; **122**(1):145–171.
51. Sun W, Ostien J, Salinger A. A stabilized assumed deformation gradient finite element formulation for strongly coupled poromechanical simulations at finite strain. *International Journal for Numerical and Analytical Methods in Geomechanics* 2013; **37**(16):2755–2788.
52. Sun W. A stabilized finite element formulation for monolithic thermo-hydro-mechanical simulations at finite strain. *International Journal for Numerical Methods in Engineering* 2015; **103**(11):798–839.
53. Biot MA. Variational Lagrangian-thermodynamics of nonisothermal finite strain mechanics of porous solids and thermomolecular diffusion. *International Journal of Solids and Structures* 1977; **13**(6):579–597.

DOI: 10.1002/nme

54. Simo JC, Hughes TJR. *Computational inelasticity*. Springer-Verlag New York: New York, 1998.
55. Radovitzky R, Ortiz M. Lagrangian finite element analysis of newtonian fluid flows. *International Journal for Numerical Methods in Engineering* 1998; **43**(4):607–619.
56. Radovitzky R, Ortiz M. Error estimation and adaptive meshing in strongly nonlinear dynamic problems. *Computer Methods in Applied Mechanics and Engineering* 1999; **172**(1):203–240.
57. Zhang X, Krischok A, Linder C. A variational framework to model diffusion induced large plastic deformation and phase field fracture during initial two-phase lithiation of silicon electrodes. *Computer Methods in Applied Mechanics and Engineering* 2016; **312**:51–77.
58. Sheng D, Sloan SW, Gens A, Smith DW. Finite element formulation and algorithms for unsaturated soils. Part I: theory. *International Journal for Numerical and Analytical Methods in Geomechanics* 2003; **27**(9):745–765.
59. Borja RI, Choo J. Cam-Clay plasticity, Part VIII: a constitutive framework for porous materials with evolving internal structure. *Computer Methods in Applied Mechanics and Engineering* 2016; **309**:653–679.
60. Choo J, White JA, Borja RI. Hydromechanical modeling of unsaturated flow in double porosity media. *International Journal of Geomechanics* 2016; **16**(6):D4016002.
61. Coussy O, Pereira JM, Vaunat J. Revisiting the thermodynamics of hardening plasticity for unsaturated soils. *Computers and Geotechnics* 2010; **37**(1):207–215.
62. Horrigmoe G, Bergan P. Incremental variational principles and finite element models for nonlinear problems. *Computer Methods in Applied Mechanics and Engineering* 1976; **7**(2):201–217.
63. Bower AF. *Applied Mechanics of Solids*. CRC Press: Boca Raton, 2009.
64. Borja RI. One-step and linear multistep methods for nonlinear consolidation. *Computer Methods in Applied Mechanics and Engineering* 1991; **85**(3):239–272.
65. Lewis RW, Schrefler BA. *The Finite Element Method in the Deformation and Consolidation of Porous Media*. Wiley, 1987.
66. Guidault PA, Belytschko T. On the L^2 and the H^1 couplings for an overlapping domain decomposition method using Lagrange multipliers. *International Journal for Numerical Methods in Engineering* 2007; **70**(3):322–350.
67. Ben Dhia H, Rateau G. Analyse mathématique de la méthode Arlequin mixte. *Comptes Rendus de l'Académie des Sciences-Series I-Mathematics* 2001; **332**(7):649–654.
68. Ferronato M, Gambolati G, Teatini P. Ill-conditioning of finite element poroelasticity equations. *International Journal of Solids and Structures* 2001; **38**:5995–6014.
69. Ferronato M, Castelletto N, Gambolati G. A fully coupled 3-D mixed finite element model of Biot consolidation. *Journal of Computational Physics* 2010; **229**:4813–4830.
70. White JA, Castelletto N, Tchelepi HA. Block-partitioned solvers for coupled poromechanics: a unified framework. *Computer Methods in Applied Mechanics and Engineering* 2016; **303**:55–74.
71. Babuška I. The finite element method with Lagrangian multipliers. *Numerische Mathematik* 1973; **20**:179–192.
72. Brezzi F, Douglas J, Marini LD. Two families of mixed finite elements for second order elliptic problems. *Numerische Mathematik* 1985; **47**:217–235.
73. Bathe KJ. The inf–sup condition and its evaluation for mixed finite element methods. *Computers and Structures* 2001; **79**(2):243–252.
74. Brezzi F, Marini L. The three-field formulation for elasticity problems. *GAMM Mitteilungen* 2005; **28**:124–153.
75. White JA, Borja RI. Stabilized low-order finite elements for coupled solid-deformation/fluid-diffusion and their application to fault zone transients. *Computer Methods in Applied Mechanics and Engineering* 2008; **197**(49):4353–4366.
76. Preisig M, Prévost JH. Stabilization procedures in coupled poromechanics problems: a critical assessment. *International Journal for Numerical and Analytical Methods in Geomechanics* 2011; **35**(11):1207–1225.
77. Choo J, Borja RI. Stabilized mixed finite elements for deformable porous media with double porosity. *Computer Methods in Applied Mechanics and Engineering* 2015; **293**:131–154.
78. Krischok A, Linder C. On the enhancement of low-order mixed finite element methods for the large deformation analysis of diffusion in solids. *International Journal for Numerical Methods in Engineering* 2016; **106**:278–297.
79. Howell JS, Walkington NJ. Inf–sup conditions for twofold saddle point problems. *Numerische Mathematik* 2011; **118**:663–693.
80. Auricchio F, Brezzi F, Lovadina C. *Mixed Finite Element Methods - Encyclopedia of Computational Mechanics*. Wiley: West Sussex, England, 2004. chap. 9. Edited by E. Stein, R. de Borst and T. J.R. Hughes. 237–279.
81. Chapelle D, Bathe K. The inf–sup test. *Computers and Structures* 1993; **47**(4–5):537–545.
82. Terzaghi K, Peck RB, Mesri G. *Soil Mechanics in Engineering Practice*. Wiley: New York, NY, 1996.
83. Bathe KJ, Hendriana D, Brezzi F, Sangalli G. Inf–sup testing of upwind methods. *International Journal for Numerical Methods in Engineering* 2000; **48**:745–760.
84. Harari I. Stability of semidiscrete formulations for parabolic problems at small time steps. *Computer Methods in Applied Mechanics and Engineering* 2004; **193**(15):1491–1516.
85. Biot MA. General theory of three-dimensional consolidation. *Journal of Applied Physics* 1941; **12**(2):155–164.
86. Rice JR, Cleary MP. Some basic stress diffusion solutions for fluid-saturated elastic porous media with compressible constituents. *Reviews of Geophysics* 1976; **14**(2):227–241.
87. Levenston ME, Frank E, Grodzinsky A. Variationally derived 3-field finite element formulations for quasistatic poroelastic analysis of hydrated biological tissues. *Computer Methods in Applied Mechanics and Engineering* 1998; **156**(1):231–246.
88. Cook RD, Malkus DS, Pleshak ME, Witt RJ. *Concepts And Applications of Finite Element Analysis: A Treatment of The Finite Element Method as Used for the Analysis of Displacement, Strain, And Stress*. Wiley: New York, NY, 1974.

DOI: 10.1002/nme

89. Rutqvist J. The geomechanics of CO_2 storage in deep sedimentary formations. *Geotechnical and Geological Engineering* 2012; **30**(3):525–551.
90. Kim J, Selvadurai APS. Ground heave due to line injection sources. *Geomechanics for Energy and the Environment* 2015; **2**:1–14.
91. Moës N, Dolbow J, Belytschko T. A finite element method for crack growth without remeshing. *International Journal for Numerical Methods in Engineering* 1999; **46**(1):131–150.
92. Hughes TJR, Cottrell JA, Bazilevs Y. Isogeometric analysis: CAD, finite elements, NURBS, exact geometry and mesh refinement. *Computer Methods in Applied Mechanics and Engineering* 2005; **194**(39):4135–4195.
93. De Luycker E, Benson D, Belytschko T, Bazilevs Y, Hsu M. X-FEM in isogeometric analysis for linear fracture mechanics. *International Journal for Numerical Methods in Engineering* 2011; **87**(6):541–565.
94. Verhoosel CV, Scott MA, de Borst R, Hughes TJR. An isogeometric approach to cohesive zone modeling. *International Journal for Numerical Methods in Engineering* 2011; **87**(1-5):336–360.
95. Watanabe N, Wang W, Taron J, Görke U, Kolditz O. Lower-dimensional interface elements with local enrichment: application to coupled hydro-mechanical problems in discretely fractured porous media. *International Journal for Numerical Methods in Engineering* 2012; **90**(8):1010–1034.
96. Réthoré J, de Borst R, Abellan MA. A two-scale model for fluid flow in an unsaturated porous medium with cohesive cracks. *Computational Mechanics* 2008; **42**(2):227–238.
97. Secchi S, Schrefler B. A method for 3-D hydraulic fracturing simulation. *International Journal of Fracture* 2012; **178**(1–2):245–258.
98. Mohammadnejad T, Khoei A. An extended finite element method for hydraulic fracture propagation in deformable porous media with the cohesive crack model. *Finite Elements in Analysis and Design* 2013; **73**:77–95.
99. de Borst R. Fluid flow in fractured and fracturing porous media: a unified view. *Mechanics Research Communications* 2016.
100. Zienkiewicz OC, Zhu JZ. The superconvergent patch recovery and a posteriori error estimates. Part 1: the recovery technique. *International Journal for Numerical Methods in Engineering* 1992; **33**(7):1331–1364.
101. Mota A, Sun W, Ostien JT, Foulk III JW, Long KN. Lie-group interpolation and variational recovery for internal variables. *Computational Mechanics* 2013; **52**(6):1281–1299.
102. Nguyen VP, Bordas SP, Rabczuk T. Isogeometric analysis: an overview and computer implementation aspects. *Mathematics and Computers in Simulation* 2015; **117**:89–116.
103. de Borst R, Réthoré J, Abellan MA. A numerical approach for arbitrary cracks in a fluid-saturated medium. *Archive of Applied Mechanics* 2006; **75**(10–12):595–606.

DOI: 10.1002/nme